Cell Reports

Article

# ADSL deficiency is a secondary mitochondrial disease affecting organelle homeostasis and ERK2/AKT signaling in a linear genotype-phenotype relation

## Graphical abstract

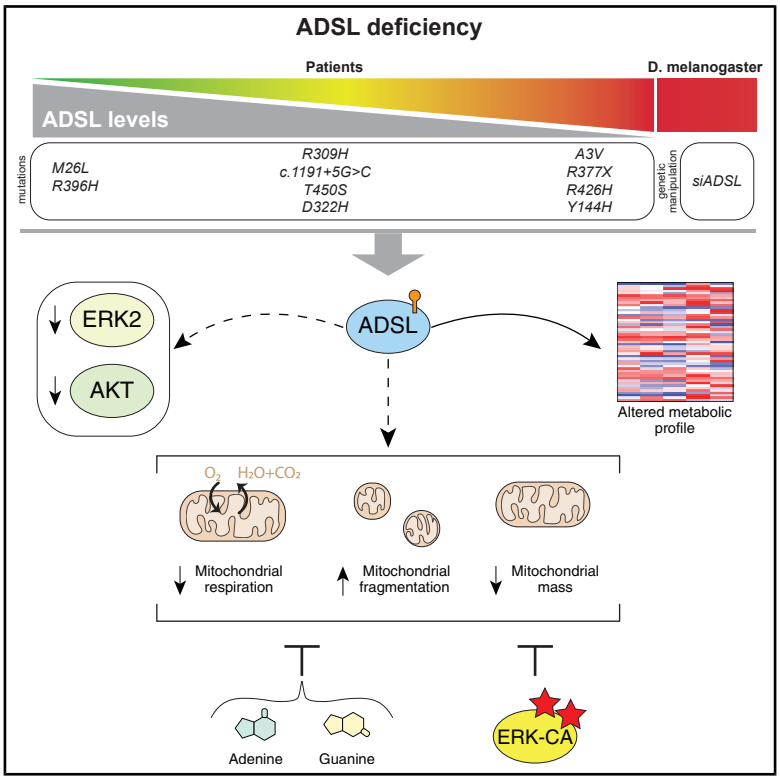


## Highlights

- ADSLd disrupts mitochondrial homeostasis; dysfunction severity linked to clinical forms
- ERK2/AKT signaling is altered in ADSLd
- ERK2 overexpression or purine supplementation partially rescues mitochondrial defects


## Authors

Matteo Bordi, Beatrice Testa, Claudia Compagnucci, ..., Marco Tartaglia, Andrea Bartuli, Francesco Cecconi

## Correspondence

matteo.bordi@unicatt.it (M.B.), francesco.cecconi@unicatt.it (F.C.)



## In brief

Bordi et al. identify mitochondrial dysfunction and ERK2/AKT impairment as hallmarks of ADSL deficiency. Mitochondrial defects correlate with disease severity and are partially rescued by ERK2-CA overexpression or purine supplementation. These findings provide insight into ADSLd pathogenesis and highlight potential therapeutic strategies targeting mitochondrial function and signaling pathways.


Bordi et al., 2025, Cell Reports *44*, 116230
September 23, 2025 
https://doi.org/10.1016/j.celrep.2025.116230

CellPress

Cell Reports

CellPress
OPEN ACCESS

Article

# ADSL deficiency is a secondary mitochondrial disease affecting organelle homeostasis and ERK2/AKT signaling in a linear genotype-phenotype relation

Matteo Bordi,[1,2,3,23,*] Beatrice Testa,[4,23] Claudia Compagnucci,[5] Fiorella Colasuonno,[4,5] Francesca Cipressa,[6] Elisabetta Betterini,[1,2] Andrea Mancini,[3] Claudia Carsetti,[7] Illari Salvatori,[8,9] Caterina Ferraina,[1,2] Ming Yang,[10] Rossella De Cegli,[11] Eugenio Del Prete,[11] Chiara Veroni,[12,13,14] Salvatore Rizza,[15] Sofia Mauri,[16] Elena Ziviani,[16] Marina Macchiaiolo,[17] Davide Vecchio,[17] Filippo Maria Panfili,[17] Teresa Rizza,[18] Gerrit Weber,[19] Rosalba Carrozzo,[18] Alberto Ferri,[8,9] Silvia Campello,[1,4] Andrea Ballabio,[11,20,21,22] Christian Frezza,[10] Gianluca Cestra,[6,7] Marco Tartaglia,[5,24] Andrea Bartuli,[17,24] and Francesco Cecconi[1,2,24,25,*]

[1]Fondazione Policlinico Universitario A. Gemelli IRCCS, Rome, Italy
[2]Università Cattolica del Sacro Cuore, Rome, Italy
[3]Cell Stress and Survival Group, Danish Cancer Institute, Copenhagen, Denmark
[4]Department of Biology, University of Rome "Tor Vergata," Rome, Italy
[5]Molecular Genetics and Functional Genomics, Bambino Gesù Children's Hospital, IRCCS, Rome, Italy
[6]University of Rome "La Sapienza," Department of Biology and Biotechnology, Rome, Italy
[7]Institute of Molecular Biology and Pathology (IBPM), National Research Council (CNR), Rome, Italy
[8]Fondazione Santa Lucia IRCCS, Rome, Italy
[9]Institute of Translational Pharmacology, National Research Council, Rome, Italy
[10]Cologne Excellence Cluster on Cellular Stress Responses in Aging- Associated Diseases (CECAD), University of Cologne, Cologne, Germany
[11]Telethon Institute of Genetics and Medicine (TIGEM), Pozzuoli, Naples, Italy
[12]Department of Molecular Medicine, Institute of Basic Medical Sciences, University of Oslo, Oslo, Norway
[13]Centre for Cancer Cell Reprogramming, Institute of Clinical Medicine, University of Oslo, Oslo, Norway
[14]Department of Molecular Cell Biology, Institute for Cancer Research, Oslo University Hospital Montebello, Oslo, Norway
[15]Redox Biology Group, Danish Cancer Institute, Copenhagen, Denmark
[16]Department of Biology, University of Padua, Padua, Italy
[17]Rare Diseases and Medical Genetics Unit, Bambino Gesù Children's Hospital, IRCCS, Rome, Italy
[18]Unit of Muscular and Neurodegenerative Disorders, Laboratory of Molecular Medicine, Bambino Gesù Children's Hospital, IRCCS, Rome, Italy
[19]Department of Pediatric Hematology, Oncology and Stem Cell Transplantation, University Hospital Würzburg, 97080 Würzburg, Germany
[20]Department of Molecular and Human Genetics and Neurological Research Institute, Baylor College of Medicine, Houston, TX, USA
[21]Medical Genetics Unit, Department of Medical and Translational Science, Federico II University, Naples, Italy
[22]Jan and Dan Duncan Neurological Research Institute, Texas Children's Hospital, Houston, TX, USA
[23]These authors contributed equally
[24]These authors contributed equally
[25]Lead contact
*Correspondence: matteo.bordi@unicatt.it (M.B.), francesco.cecconi@unicatt.it (F.C.)
https://doi.org/10.1016/j.celrep.2025.116230

## SUMMARY

Adenylosuccinate lyase deficiency (ADSLd) is a rare autosomal recessive purine metabolism disorder with several clinical manifestations. While toxic substrate accumulation is a known hallmark, no additional molecular mechanisms have been established. Here, we show that ADSLd is associated with mitochondrial dysfunction, including increased fragmentation, impaired respiration, and reduced ATP production. The severity of mitochondrial impairment correlates with ADSLd pathology, especially in mitochondria-dependent tissues. We also identify defects in mitochondrial dynamics and transport linked to ERK2 and AKT suppression. Notably, overexpressing constitutively active ERK2 or supplementing purine intermediates partially rescues the mitochondrial phenotype. These findings suggest an alternative disease mechanism and highlight mitochondrial metabolism as a potential therapeutic target in ADSLd.

## INTRODUCTION

Adenylosuccinate lyase deficiency (ADSLd) (OMIM#103050) is an autosomal recessive deficit of purine metabolism caused by biallelic mutations in the *ADSL* gene (OMIM#608222).[1] The disease, first described in 1984, is characterized by wide clinical variability, ranging from a fatal neonatal form, which is characterized by encephalopathy, intractable seizures, and respiratory

failure, to a very mild phenotype characterized by isolated psychomotor delay[2–4] (Table S1). ADSL functions as a homotetramer, catalyzing two non-sequential steps of *de novo* purine synthesis: the conversion of succinylaminoimidazolecarboxamide ribotide (SAICAR) into aminoimidazolecarboxamide ribonucleotide (AICAR), and formation of adenosine monophosphate (AMP) from adenylosuccinate (S-AMP).[1,5,6] *ADSL* mutations cause loss of function (LoF) of the enzyme, leading to an intracellular accumulation of SAICAR and S-AMP, which are respectively dephosphorylated into succinylaminoimidazole carboxamide riboside (SAICAr) and succinyladenosine (S-Ado), with both therefore detectable in patients' body fluids.[1,2] ADSL is also involved in the purine nucleotide cycle, balancing the ATP/AMP ratio.[1,7,8] Additionally, by generating fumarate in both reactions, ADSL contributes to the tricarboxylic acid (TCA) cycle.[1,5]

ADSLd is a rare disease, with fewer than 100 cases reported thus far and a prevalence estimated at 1 in 1.25 million.[1,9] Over 50 different *ADSL* deleterious variants have been described, mostly representing missense variants.[1,5] Based on the clinical presentation and S-Ado/SAICAr ratio in cerebrospinal fluid (CSF), four phenotypic categories have been defined: fatal neonatal (ratio <1), severe (ratio ~1), mild (ratio >2) and very mild form (ratio >3.5)[1,10].

The molecular mechanisms underlying ADSLd etiology are largely uncharacterized.[1,5] Hypotheses include the toxicity of SAICAR, S-AMP, SAICAr, and/or S-Ado accumulation, deficiency of purine nucleotides, or impairment of the purine cycle in muscle and brain.[1] Of note, the severity of the disease appears to be inversely correlated with the ability to assemble the cellular structure that regulates the purine pathway, a metabolon known as purinosome.[11,12] To ensure robust validation, we used three complementary models derived from ADSLd patients: primary fibroblasts (non-transformed), induced pluripotent stem cells (iPSCs) and iPSC-derived neurons to model neural cells, and Epstein-Barr virus-immortalized lymphoblastoid cell lines (EBV-LCLs) for standardized genetic and biochemical analyses. These systems provide a comprehensive view of the mitochondrial phenotype. We show that ADSL mutations reduce mRNA and protein levels in a severity-dependent manner. Patient-derived cells exhibit impaired mitochondrial homeostasis, which leads to elevated cell death in both iPSCs and iPSC-derived motor neurons. These phenotypes are recapitulated in a *Drosophila melanogaster* model with RNAi-mediated ADSL knockdown in tissues including muscle. We also observe reduced ERK2 and AKT signaling in patient and fly models. Notably, tissue-specific expression of constitutively active ERK in ADSL-RNAi flies partially rescues lethality and mitochondrial defects. Finally, based on purine dysregulations revealed by metabolomics, adenine or guanine supplementation restores mitochondrial mass, activity, and morphology in ADSLd fibroblasts.

## RESULTS

### *ADSL* gene mutations affect ADSL protein levels in patient cells

To assess the correlation between *ADSL* gene expression and disease severity, we analyzed ADSL mRNA and protein levels in primary fibroblasts from patients with very mild, mild, severe, and fatal neonatal forms, and in EBV-LCLs from patients with mild forms (Figures 1A and 1B, S1A–S1C). Patient phenotypes were classified based on clinical presentation (including developmental delay, muscle tone abnormalities, seizure burden, and cerebral atrophy or hypomyelination), and S-Ado/SAICAr ratio in CSF, as previously reported.[1,10,13] Phenotype severity, genotype, and sex are reported in Figure S1A. Control cells (CTR) were derived from age- and sex-matched healthy donors. ADSL mRNA and protein levels were significantly reduced in cell lines from mild, severe, and fatal neonatal cases (Figures 1A and 1B; S1B and S1C). Notably, ADSL protein levels in fibroblasts decreased in accordance with clinical severity (Figure 1B). To investigate whether protein loss was due to degradation, we tested ADSL stability in EBV-LCLs using time-course treatments with the proteasome inhibitor MG132, the lysosomal V-ATPase inhibitor concanamycin A (ConA),[14] or both (Figures S1D–S1G). These treatments did not significantly increase ADSL levels in patient cells.

Moreover, we measured protein half-life using cycloheximide (CHX) chase assay. After 10 h of CHX treatment, ADSL levels remained consistent across pathogenic variants, indicating that it is a relatively stable protein (Figures S1H and S1I). These data suggest that biallelic *ADSL* mutations impair transcription and/or translation, regardless of mutation type. To explore possible functional relevance of ADSL expression, we used the GeneBridge platform.[15] Alongside enrichment for nucleotide biosynthesis and purine metabolism, we unexpectedly found ADSL expression in brain and muscle positively correlated with genes involved in mitochondrial processes, including respiratory electron transport, mitochondrial translation, protein import, and the mitochondrial protein complex (Figures 1C and 1D). Given this and the fact that brain and muscle (tissues highly dependent on mitochondrial function) are most affected in ADSLd,[1] we decided to assess mitochondrial shape and functions in ADSLd.

### *ADSL* pathogenic variants affect mitochondrial dynamics and functions in patient cells

First, we evaluated the mitochondrial network in patient fibroblasts by immunofluorescence analysis and found that ADSLd mitochondria are fragmented (Figures 2A–2C), with a consistent co-evolution between the degree of fragmentation and the disease severity.

We next assessed mitochondrial respiration in very mild and mild-ADSLd fibroblasts using Seahorse assay (Figures 2D–2F), as severe and fatal neonatal cells exhibited extremely slow growth and could not be analyzed by this method. Notably, severe-form cells showed increased senescence compared to control and fatal neonatal cells (Figure S2A). Interestingly, we observed a reduction in basal respiration and mitochondria-dependent ATP production in cells from mild-ADSLd patients, but not in the very mild ones (Figures 2D and 2E). However, we assessed the kinetics of ATP production from mitochondrial oxidative phosphorylation (mitoATP) and glycolysis (glycoATP). The resulting ATP rate index revealed that, in all three ADSL-deficient cell types analyzed, there was a marked decrease in ATP generated through oxidative phosphorylation (OXPHOS), accompanied by a compensatory increase in glycolytic ATP production (Figure 2F). These data were confirmed in

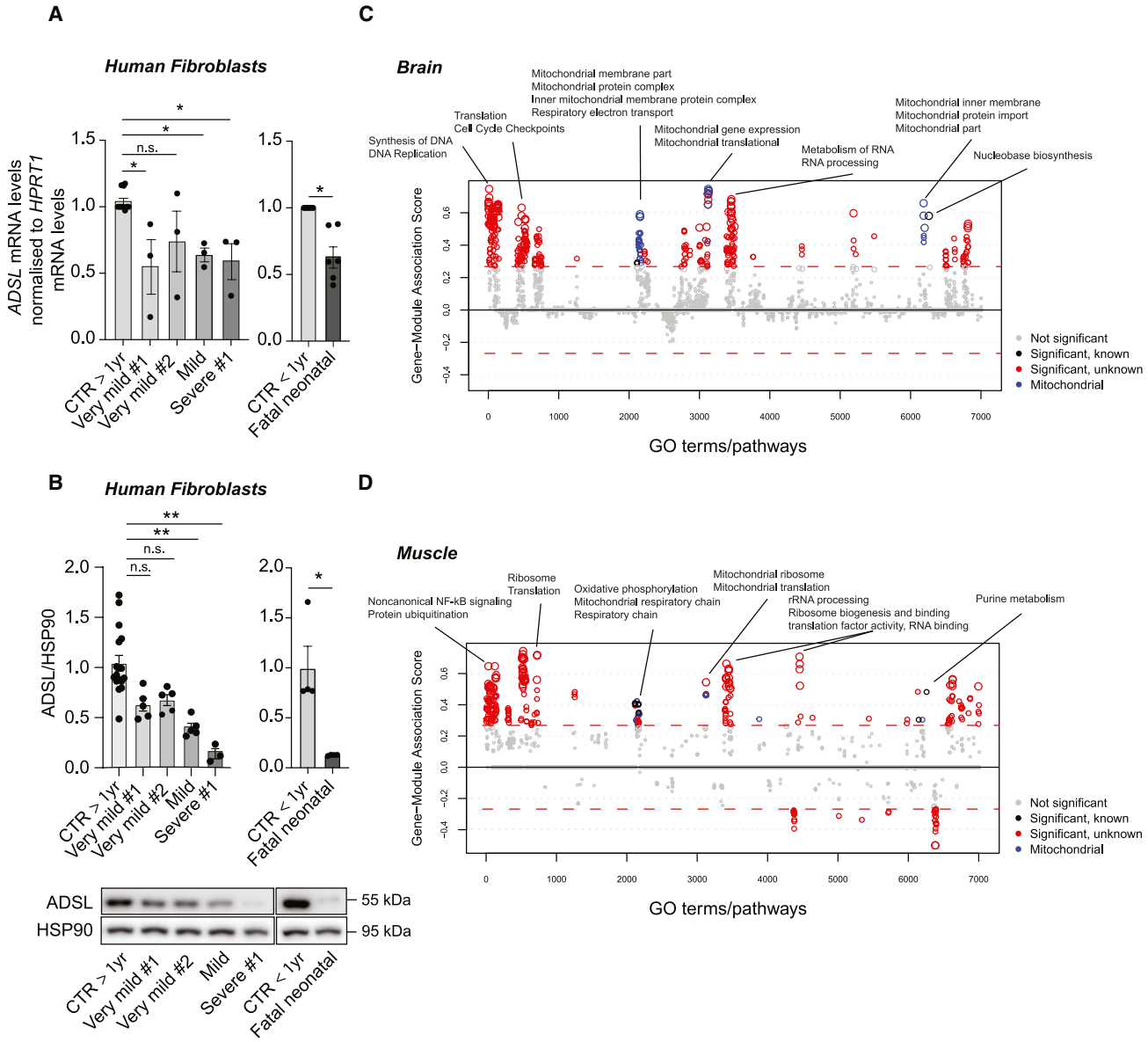


**Figure 1. Genetic variation affects *ADSL* expression in patients' fibroblasts**

(A) *ADSL* mRNA expression in patients' fibroblasts was assessed by qPCR and normalized against HPRT1. mRNA levels used for the control condition were pooled from three independent WT fibroblast lines. Values are mean ± SEM ($n \geq 3$).

(B) Western blotting analysis for ADSL in patients' fibroblasts. Densitometry analysis of ADSL normalized against HSP90 is also shown (top). Protein lysates for the control condition were pooled from three independent WT fibroblast lines. Values are mean ± SEM ($n \geq 3$).

(C and D) Gene Ontology (GO) terms and pathways associated with ADSL expression in human brain (C) and muscle (D). The red dashed line marks significance (Gene-module association score [GMAS] $\geq 0.268$ or $\leq -0.268$). Terms are grouped by similarity: gray dots indicate non-significant associations, black dots represent known ADSL-related terms, blue highlights mitochondrial-related terms, and red indicates newly associated significant terms. Dot size reflects the GMAS value (data from https://systems-genetics.org).

Statistical analyses were performed using Kruskal-Wallis test with Dunn's multiple comparisons test or Mann-Whitney test when two groups were compared. $^{*}p < 0.05$, $^{**}p < 0.01$, $^{***}p < 0.001$, and $^{****}p < 0.0001$.

patient-derived EBV-LCLs (Figures S2B and S2C). Of note, silencing of *ADSL* in neuroblastoma-derived SH-SY5Y cells resulted in a more substantial suppression of the mitochondrial respiration capacity (Figures S2D and S2E), as also previously reported on hepatocellular carcinoma cell lines.[16] Then, we measured the mitochondrial membrane potential and mitochondrial mass in patient-derived EBV-LCLs. All mild-ADSLd cell lines showed reductions in both parameters (Figure S2F). To investigate whether ADSL deficiency affected mitochondrial genome maintenance, we measured the mitochondrial DNA

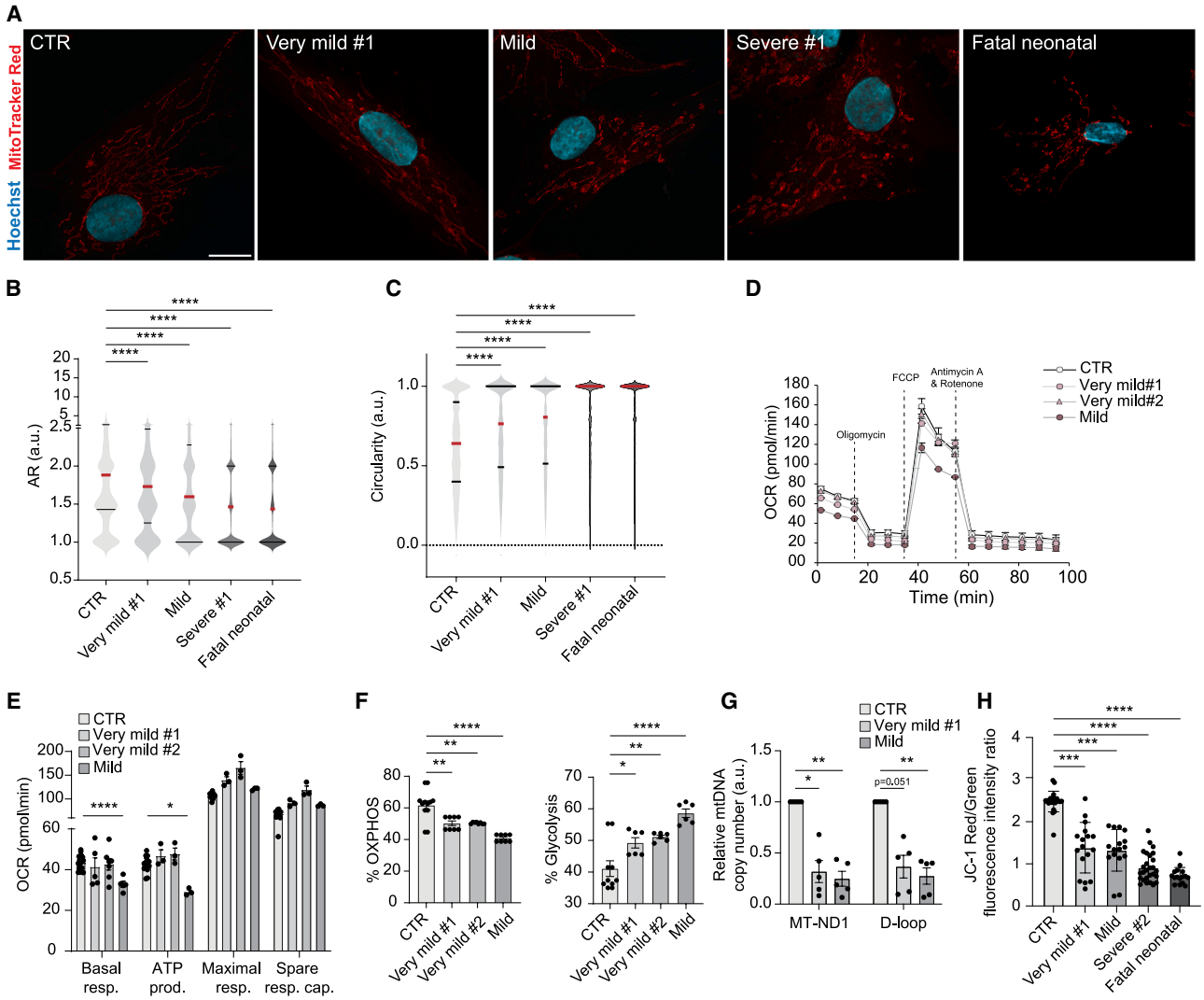


**Figure 2. Mitochondrial dysfunction and mtDNA depletion in ADSLd patient-derived models**

(A) Representative confocal images of the mitochondrial network of patients' fibroblasts revealed by MitoTracker Red CMXRos; Hoechst (blue) was used to mark nuclei. Scale bar, 20 μm.

(B and C) Mitochondrial length (aspect ratio [AR]) and circularity analyses were performed using ImageJ software. In the violin plots, the red bars indicate median values, while the black bars (which may appear blue depending on rendering) represent the first and third quartiles. Values are mean ± SEM ($n = 3$; $n > 30$ cells analyzed).

(D) Oxygen-consumption rate (OCR) of patients' fibroblasts measured by Seahorse assay ($n = 3$).

(E) Basal, ATP-coupled (ATP prod.), maximal respiration, and spare respiratory capacity of the cells in (D). Values are mean ± SEM ($n \geq 3$).

(F) ATP production rate from both mitochondrial and glycolytic pathways in patients' fibroblasts. Values are mean ± SEM ($n \geq 3$).

(G) Relative mtDNA content was assessed in very mild #1 and mild ADSLd fibroblast lines by measuring the copy number of *MT-ND1* gene and D loop region using qPCR. Values are relative to control fibroblasts, normalized against genomic *β-ACTIN* levels, and reported in arbitrary units (a.u.). Values are mean ± SEM ($n = 5$).

(H) Mitochondrial membrane potential by JC-1 staining was performed by immunofluorescence analysis on ADSLd iPSCs under basal condition. JC-1 red/green fluorescence intensity ratio is shown. Values are mean ± SEM ($n \geq 16$).

Statistical analyses were performed using one-way ANOVA with Dunnett's multiple comparisons test or Kruskal-Wallis test with Dunn's multiple comparisons test. $^{*}p < 0.05$, $^{**}p < 0.01$, $^{***}p < 0.001$, and $^{****}p < 0.0001$.

(mtDNA) content in patient-derived fibroblasts by monitoring the copy number of the NADH-ubiquinone oxidoreductase chain 1 (*MT-ND1*) gene and the displacement loop (D loop) region via qPCR. We observed a significant reduction in mtDNA content in both very mild #1 and mild ADSL-deficient fibroblast lines compared to controls (Figure 2G). A similar decrease was also detected in EBV-LCLs derived from ADSLd patients, confirming the consistency of this molecular phenotype across cell types (Figure S2G). Next, to assess whether this reduction in mtDNA content was associated with impaired mitochondrial gene expression, we measured mRNA levels of the mitochondrial-encoded genes ATP synthase F(0) complex subunit a (*ATP6*),

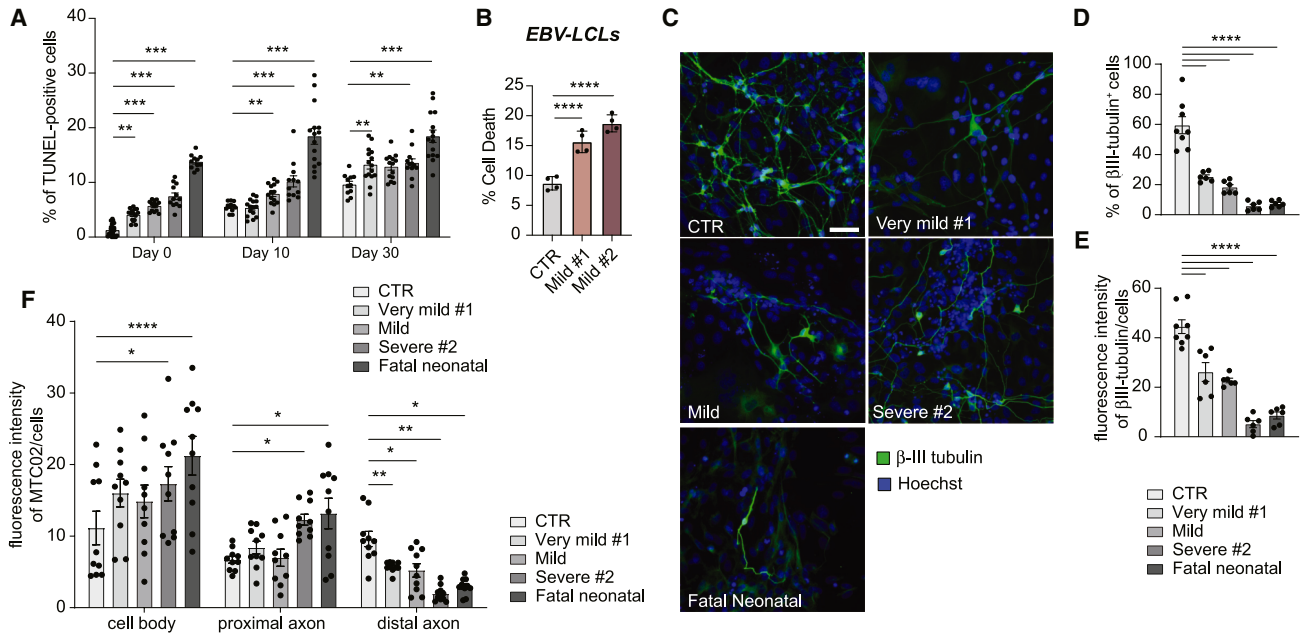


**Figure 3. ADSLd iPSCs manifest increased cell death and impaired differentiation into neurons**

(A) iPSC apoptosis detection during neuronal differentiation using the TUNEL assay, displayed as the percentage of TUNEL-positive cells. Values are mean ± SEM ($n \geq 10$).

(B) Percentage of apoptotic cells in patients' EBV-LCLs, as determined by flow cytometry following propidium iodide (PI) staining. PI-positive cells were quantified to assess cell death. Values are mean ± SEM ($n = 4$).

(C) Immunofluorescence analysis of the neuronal differentiation potential using β-III tubulin (green) as marker for differentiated neurons. Scale bar, 50 μm.

(D and E) The percentage of β-III tubulin-positive cells (D) and the fluorescence intensity of β-III tubulin per cells (E) are also shown. Values are mean ± SEM ($n = 6$).

(F) Quantification of the fluorescence intensity levels of mitochondria, marked with anti-MTC02, in different portions of ADSLd-derived motor neurons. β-III tubulin (green) was used to mark differentiated neurons. Values are mean ± SEM ($n = 10$).

Statistical analyses were performed using one-way ANOVA with Dunnett's multiple comparisons test. *$p < 0.05$, **$p < 0.01$, ***$p < 0.001$, and ****$p < 0.0001$.

NADH-ubiquinone oxidoreductase chain 3 (*ND3*), and cytochrome *c* oxidase subunit 2 (*COXII*) by qPCR. Despite mtDNA depletion, no consistent transcriptional changes were detected across the analyzed cell lines (Figures S2H and S2I). To further explore potential compensatory mechanisms, we examined levels of mitochondrial dynamics regulators such as optic atrophy 1 (OPA1), dynamin-related protein 1 (DRP1; total and phosphorylated), and mitofusin 2 (MFN2). These proteins were unchanged in ADSLd EBV-LCLs (Figure S2J). In addition, we found no alterations in OXPHOS complex levels, oxidative stress, or mitophagy flux that could explain the reduced mitochondrial mass (Figures S2K–S2M).

Last, we generated iPSCs from patient-derived fibroblasts (Figures S2N and S2O) and measured mitochondrial membrane potential with the JC-1 compound after its activity validation (Figure S2P). In agreement with our previous findings, the mitochondrial potential of patient-derived iPSCs was significantly decreased compared to controls (Figures 2H and S2Q), confirming a decline in mitochondrial health also in these cells.

## ADSLd iPSCs exhibit increased cell death and impaired neuronal differentiation

Based on these results, we next hypothesized that the mitochondrial function deficit observed in ADSLd cells might influence iPSC differentiation into neurons, during which cells undergo profound metabolic reprogramming to switch from glycolytic to OXPHOS metabolism.[17] Thus, we induced differentiation of iPSCs into motor neurons and evaluated cell death. Remarkably, all patient-derived iPSCs exhibited a substantial basal increase in the apoptosis rate in all the examined stages of differentiation, including neuronal progenitor cells (day 10) and differentiated neurons (day 30), as we also observed in ADSLd EBV-LCLs (Figures 3A and 3B). Moreover, patient-derived iPSCs exhibited a decline in neuronal yield and differentiation efficiency, with more pronounced defects in severe and fatal neonatal forms, correlating with disease severity (Figures 3C–3E; S3A). Additionally, differentiated neurons from ADSLd cells exhibited a marked decrease in neurite length (Figure S3B). Since functional mitochondria are dynamic and move bidirectionally along neuronal processes, while damaged ones are transported to the soma for repair or degradation,[18] we analyzed mitochondrial distribution in neurons. Compared to controls, severe and fatal neonatal iPSC-derived neurons showed significant mitochondrial accumulation in the soma and proximal axon (Figure 3F). This alteration in mitochondrial localization and neuronal differentiation appeared to mirror the severity of the neurological phenotype observed clinically. Notably, mitochondrial content was significantly reduced in the distal axons across all cell lines (Figure 3F).

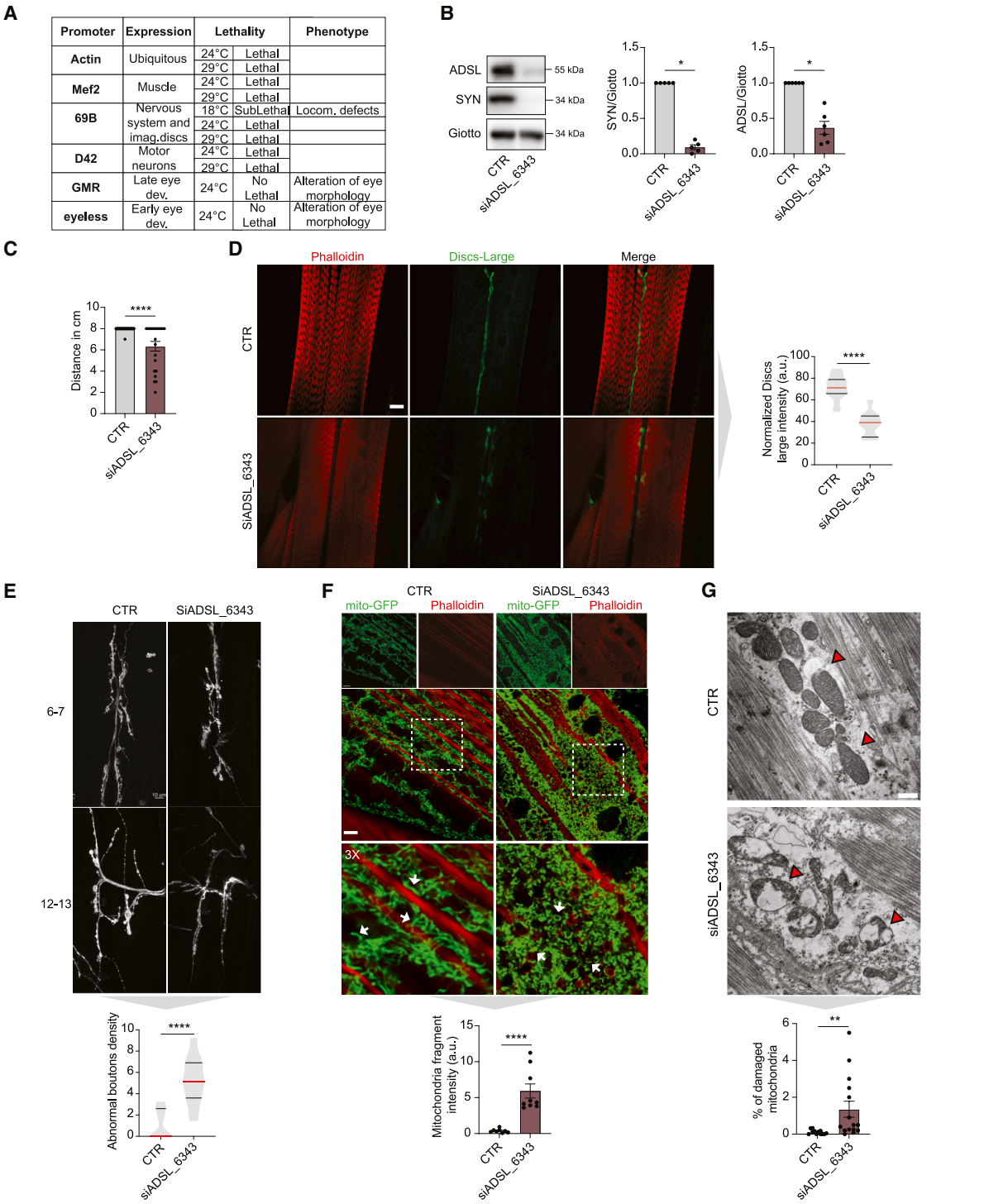


| Promoter | Expression | Lethality | | Phenotype |
|---|---|---|---|---|
| Actin | Ubiquitous | 24°C | Lethal | |
| | | 29°C | Lethal | |
| Mef2 | Muscle | 24°C | Lethal | |
| | | 29°C | Lethal | |
| 69B | Nervous system and imag.discs | 18°C | SubLethal | Locom. defects |
| | | 24°C | Lethal | |
| | | 29°C | Lethal | |
| D42 | Motor neurons | 24°C | Lethal | |
| | | 29°C | Lethal | |
| GMR | Late eye dev. | 24°C | No Lethal | Alteration of eye morphology |
| eyeless | Early eye dev. | 24°C | No Lethal | Alteration of eye morphology |

**Figure 4. *Drosophila* model of ADSL deficiency**

(A) The table lists all GAL4 promoters employed to drive tissue-specific expression of UAS-ADSL RNAi. For each driver, we indicate the target tissue, the tested temperature, whether the knockdown resulted in lethality or caused any phenotype.

(B) Western blotting analysis of ADSL and SYN proteins in *Drosophila* larvae expressing ADSL RNAi in muscles. Densitometry analysis of ADSL and SYN normalized against Giotto is shown (right). Values are mean ± SEM ($n \geq 5$).

(C) Analysis of locomotion activity of adult flies expressing ADSL RNAi in neurons (69B-GAL4). Values are mean ± SEM ($n \geq 22$ flies from three independent experiments).

*(legend continued on next page)*

### *ADSL* knockdown in *Drosophila* triggers mitochondrial alterations

To further investigate the role of ADSL in mitochondrial homeostasis *in vivo*, we silenced the *Drosophila* ortholog of human *ADSL* (*dADSL*), which shares 67% of identity with the human gene (DIOPT Ortholog Finder),[19] using the UAS-GAL4 system (Figure 4A). Two independent RNAi constructs targeting dADSL were tested under the eyeless-GAL4 driver at 29°C. Both caused significant eye-size reduction compared to controls, with RNAi line 6343 showing a stronger phenotype and more efficient knockdown (Figures S4A and S4B). Therefore, SiADSL_6343 was selected for subsequent experiments.

We next validated the efficiency of this construct expressing it in fly larval muscles under Mef2-GAL4 driver at 25°C and confirmed *dADSL* knockdown by western blotting analysis (Figure 4B). This construct caused adult fly lethality under all drivers tested (Figure 4A), except for glass multimer reporter (GMR) and eyeless (both at 25°C and 29°C), consistent with embryonic lethality previously reported in ADSL knockout mice.[20] Moreover, repression of *dADSL* under the control of neuronal and imaginal discs driver 69B-GAL4 at 18°C, a temperature that slows down fly metabolism, reduces the levels of GAL4 transcription factor and decreases RNAi expression, leading to defective locomotion compared to controls (Figure 4C).

Furthermore, the expression of *dADSL* RNAi in larval muscles led to a marked reduction in the levels of synapsin (SYN) (Figure 4B), which controls synaptic activity and budding of synaptic boutons at the neuromuscular junction (NMJ).[21] Thus, we examined the NMJs in these larvae, and we observed severe alteration of their morphology, as indicated by a significant decrease in the post-synaptic marker Discs-large, which localizes in the infolding of the post-synaptic membrane of the subsynaptic reticulum (Figure 4D). To further assess NMJ architecture, we performed immunofluorescence staining with anti-horseradish peroxidase (HRP) to label presynaptic membranes. This analysis revealed pronounced alterations in bouton morphology, with a significant increase in abnormally enlarged boutons compared to controls (Figure 4E). Notably, co-expression of a mitochondrially targeted GFP (mito-GFP) and the dADSL RNAi construct in larval muscle revealed markedly increased mitochondrial fragmentation (Figure 4F), consistent with observations in ADSLd-patient-derived cells. To further investigate mitochondrial architecture, we used transmission electron microscopy (TEM) to examine muscle tissue. *ADSL* downregulation strongly altered mitochondrial structures, including disorganized cristae structure (as indicated by the red arrowheads in Figure 4G), and a significant accumulation of damaged mitochondria compared to controls (Figure 4G). These findings underscore the critical role of ADSL in regulating mitochondrial morphology and function *in vivo* during development.

### ERK2 and AKT signaling is impaired in ADSLd cells

The purine-synthesis pathway is tightly regulated both enzymatically and transcriptionally. Besides the essential role of ERK and AKT in controlling cell proliferation, differentiation, and apoptosis,[22,23] these kinases positively regulate purine biosynthesis by phosphorylating phosphoribosylformylglycinamidine synthase (PFAS) and transketolase (TKT), respectively,[22,24–26] two enzymes that are upstream of ADSL.[27] Indeed, ERK2 activation, through PFAS, enhances *de novo* purine synthesis pathways, thereby augmenting the availability of essential intermediates such as AMP and GMP.[26] Additionally, ERK2 can regulate mitochondrial energy production[28] and mitochondrial morphology.[29] Similarly, AKT is a key regulator of mitochondrial function, promoting glucose uptake, enhancing respiratory efficiency, and increasing mitochondrial ATP production.[30,31]

Thus, we decided to evaluate the AKT and ERK1/2 signaling pathway in patient cells. Interestingly, mild-form ADSLd fibroblasts and EBV-LCLs displayed a significant decrease in the steady-state activation of both ERK2 and AKT (Figures 5A, 5B, S5A, and S5B). This finding supports the idea that ADSL impairment may affect these two kinases and that the degree of their inhibition may correlate with the severity of the clinical ADSLd phenotype.

We then examined ERK1/2 and AKT activation under specific stimuli. Given their responsiveness to glucose availability,[32,33] fibroblasts were glucose starved for 24 h and harvested 20 min after glucose reintroduction (Figures 5C–5E). After glucose deprivation, a moderate decrease in the activation of AKT and ERK2 was observed in mild-ADSLd cells (Figures 5D and S5C). Hence, glucose reintroduction could not restore ERK1/2 and AKT activation in mild-ADSLd cells when compared to healthy

(D) NMJ (muscle 6 and 7) immunofluorescence analysis of third-instar larvae on expressing d*ADSL* RNAi under Mef2-GAL4 driver. NMJs were co-stained with fluorescent labeled phalloidin (marker of muscle actin fibers) and anti-Discs-large (marker of subsynaptic reticulum). Discs-large signal intensity was measured and divided by NMJ total area for normalization. Around 10 NMJs for each genotype were analyzed (control $n = 9$ NMJs, ADSL RNAi $n = 12$ NMJs). All crosses for the NMJ analysis were held at 29°C. Scale bars, 20 μm. The violin plots (right) report median (dashed lines), first and third quartile (dotted lines), and density plot (outside lines).

(E) Immunofluorescence analysis of third-instar-larva NMJs on muscle 6 and 7 of flies expressing *dADSL* RNAi under Mef2-GAL4 driver. Anti-HRP was used to highlight presynaptic membranes and representative images are presented. Few representative NMJs on muscle 12 and 13 were also added. The area of all boutons of each NMJ was measured and normalized by the length of the junction. The area of each abnormal bouton above a fixed threshold (area > 1,000 a.u.) was considered and summed. Around 20 NMJs for each genotype were analyzed (control $n = 19$ NMJs, ADSL RNAi $n = 19$ NMJs). Scale bars, 10 μm. The violin plots (bottom) report median (dashed lines), first and third quartile (dotted lines), and density plot (outside lines).

(F) Immunofluorescence analysis of the mitochondrial network of *Drosophila* larval muscles expressing ADSL RNAi and mito-GFP reporter (green); phalloidin (red) was used to mark actin filaments. Scale bar, 10 μm. The measure of mitochondrial fragmentation is also shown (left). Values are mean ± SEM ($n \geq 7$).

(G) Representative transmission electron microscopy (TEM) images of larval muscles expressing ADSL RNAi under Mef2-GAL4 driver. Mitochondria are highlighted with red arrowheads. Scale bar, 500 nm. Quantification of mitochondrial fragmentation is shown (bottom) and was assessed by analyzing multiple independent electron microscopy (EM) images per condition and defined as the percentage of damaged or fragmented mitochondria relative to the total number of mitochondria per field (from three independent experiments).

Values are mean ± SEM. Statistical analyses were performed using unpaired Student's t test or Wilcoxon matched-pairs signed rank test. $^{*}p < 0.05$, $^{**}p < 0.01$, and $^{****}p < 0.0001$.

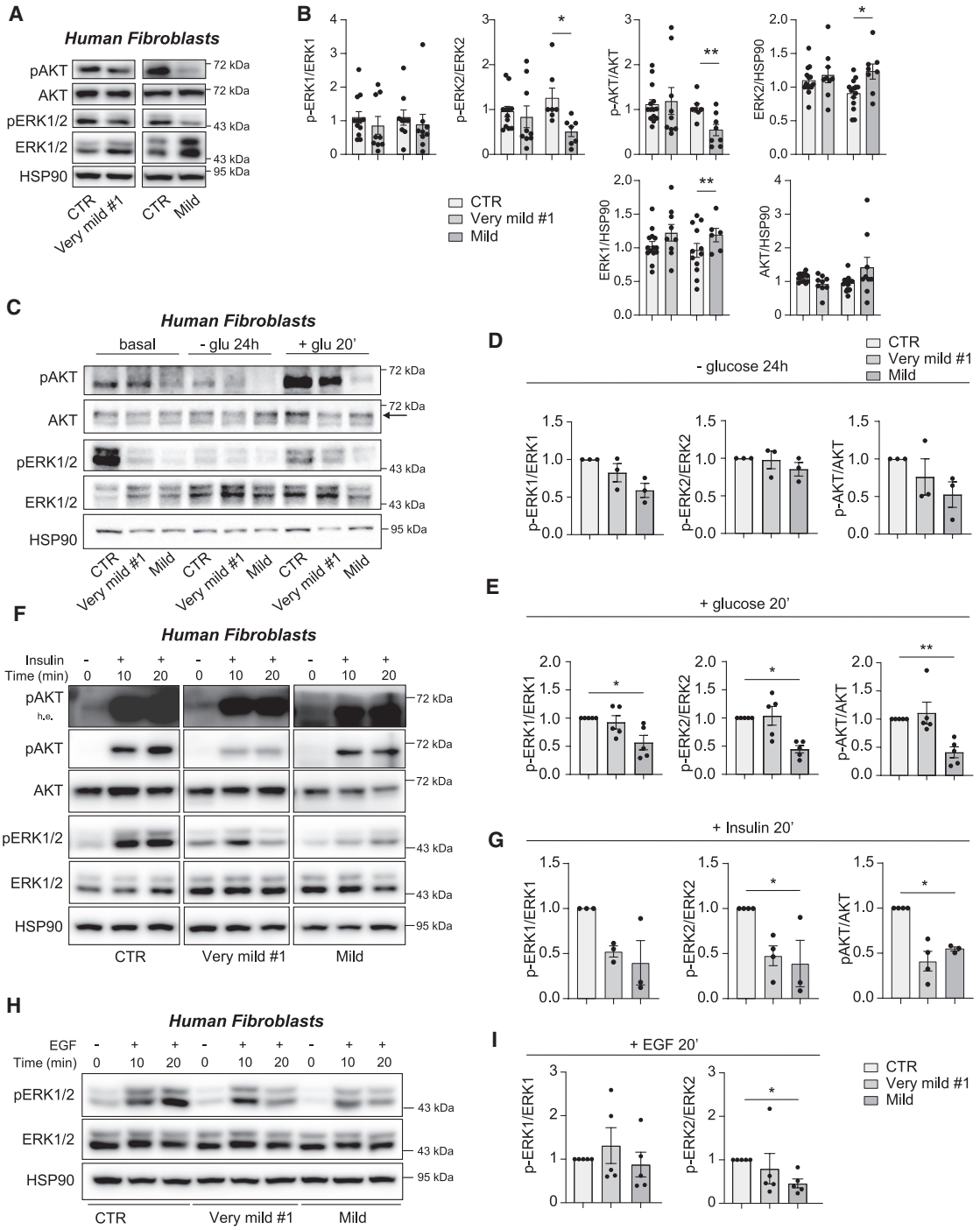


**Figure 5. AKT and ERK2 are affected by *ADSL* pathogenic variants**

(A and B) (A) Western blotting analysis for AKT$^{pThr308}$, AKT, ERK1/2$^{pThr202/Tyr204}$, and ERK1/2 in patients' fibroblasts in basal condition. Densitometry analyses of AKT$^{pThr308}$ normalized against AKT, ERK1/2$^{pThr202/Tyr204}$ normalized against ERK1/2, and AKT and ERK1/2 normalized against HSP90 are also shown in (B). Values are mean ± SEM ($n \geq 8$).

(C–E) (C) Western blotting analysis for AKT$^{pThr308}$, AKT, ERK1/$^{2pThr202/Tyr204}$, and ERK1/2 in fibroblasts derived from very Mild #1 and mild patients and control after 24 h of glucose starvation (– glu 24h) and 20 min of glucose reintroduction (+ glu 20′, obtained by using DMEM containing 4,500 mg/L D-glucose). Densitometry analyses of AKT$^{pThr308}$ normalized against AKT and ERK1/2$^{pThr202/Tyr204}$ normalized against ERK1/2 are also shown in (D) for the "– glucose 24h" condition and in (E) for the "+ glucose 20′" condition. Values are mean ± SEM ($n$ = 3).

*(legend continued on next page)*

controls, indicating defective glucose sensing (Figures 5E and S5C). This impairment was confirmed in EBV-LCLs, which exhibited similarly blunted responses to glucose reintroduction (Figures S5D and S5E), suggesting a conserved signaling defect across ADSLd models. To further investigate these signaling pathways, we next treated ADSLd fibroblasts with insulin or epidermal growth factor (EGF), to promote specific activation of the two kinases.[22,23] Although fibroblast cells from the very mild and mild forms were able to respond to insulin treatment, at the time point when these kinases reach their maximum activity in controls (20 min), we did not observe any further increase of ERK2 and AKT activity in mild-ADSLd cells (Figures 5F, 5G, and S5F). In addition, EGF treatment, which specifically promotes the activation of ERK1/2, showed a decreased ability to activate ERK2 in the mild-form cells (Figures 5H, 5I, and S5G).

These results suggest that ERK1/2 and AKT signaling, as well as the capacity of cells to respond to external stimuli, were adversely affected in the more severe forms of ADSLd, indicating that they acquired a diminished ability to adapt to physiological or metabolic changes or stress.

## ERK overexpression rescues mitochondrial alterations in the ADSLd *Drosophila* model and patient-derived cells

Given the negative effects of *ADSL* pathogenic variants on ERK2 and AKT signaling pathways, we measured the protein levels of both kinases in *Drosophila* larvae expressing *dADSL* RNAi construct in muscles (*Drosophila* expresses a single ERK isoform) (rolled). Interestingly, levels of both kinases were strikingly downregulated (Figure 6A), confirming *in vivo* the evidence obtained in ADSLd patient cells.

Thus, we tested whether the upregulation of *Drosophila* ERK affected the phenotypical alterations caused by ADSLd. By using the same UAS-GAL4 system, we expressed either wild-type (ERK-WT) or constitutively active (ERK-CA) forms of ERK (*rolled*) in muscles, together with the *dADSL* RNAi construct. Strikingly, only ERK-CA partially rescued adult lethality, increasing survival from 0% to 18%, and supporting a central role for ERK in this pathway (Figure 6B). ERK-CA also restored mitochondrial morphology in motor neurons of larvae expressing the RNAi (Figure 6C). We next expressed ERK-WT and ERK-CA in mild-ADSLd EBV-LCLs and control cells. Both constructs significantly increased mitochondrial membrane potential and mass (Figures 6D and S6), consistent with *in vivo* results. Finally, we measured mtDNA copy number under the same conditions. ERK-CA expression significantly rescued mtDNA levels in mild ADSLd EBV-LCLs but had no effect in controls (Figure 6E). Together, these findings establish a direct link between ADSL deficiency, ERK suppression, and mitochondrial dysfunction and suggest that targeting ERK activity may offer a potential therapeutic strategy for ADSLd.

## Metabolomic profiling of ADSLd patients' fibroblasts

To further investigate the role of altered metabolism and mitochondrial homeostasis in ADSLd, we performed metabolomic profiling on patient-derived fibroblasts (Figure 7A). As expected, metabolite set enrichment analysis (MSEA) revealed purine metabolism defects (Figure 7B), along with changes in the urea cycle and aspartate, glycine, and serine pathways. These alterations were confirmed in mild-ADSLd EBV-LCLs, which also showed defects in glycolysis and the mitochondrial electron transport chain (Figures S7A and S7B). We then analyzed the *de novo* purine synthesis pathway in more detail. S-AMP and S-Ado levels were markedly elevated in mild and severe fibroblasts, and to a lesser extent in the very mild form, while remaining nearly undetectable in controls (Figure 7C). Furthermore, fumarate levels, produced as a secondary metabolite in both ADSL-catalyzed reactions,[8] remained unchanged (Figure 7A). Hence, S-Ado and S-AMP emerged as the only consistent markers across ADSLd subtypes, while other metabolic changes were form specific, likely reflecting distinct compensatory responses. By this analysis, we observed a defect in the adenine arm of purine biosynthesis in the severe form, coupled with a significant decrease in the levels of adenosine and AMP (Figure 7C). By contrast, the levels of guanine and guanosine decreased primarily in the mild form (Figure 7C). Interestingly, guanine and guanosine were also significantly decreased in the mild form of ADSLd EBV-LCLs derived from patients, compared to control cells; unfortunately, adenine was not detected by our experimental conditions (Figures S7A and S7C). Moreover, GTP and GDP levels were increased in the ADSLd mild form. In principle, since the *de novo* purine synthesis is impaired, GMP and AMP could also be generated via purine salvage pathways,[34] partially compensating for ADSLd. Thus, we also performed metabolomic analyses using $^{13}$C-glycine on fibroblast samples from very-mild-, mild-, and severe-form patients. Glycine was chosen because of its role in the *de novo* purine synthesis, where it contributes with three atoms.[12] Labeled fractions showed a visible trend toward reduced labeled ATP, ADP, guanosine, and adenosine (m + 2); although these changes were not statistically significant in ADSLd cells, except for adenosine in the severe-form sample, this analysis suggests an altered purine metabolism in patient cells (Figure S7C).

The observed adenine and guanine dysregulation led us to test whether these arms of purine biosynthesis could contribute to the mitochondrial impairment described in our models. In fact, it has been described that guanosine supplementation can restore mitochondrial fusion in cancer cells[35] and that adenosine improves mitochondrial function in Friedreich's ataxia.[36] Furthermore, adenine supplementation enhances cell growth in disorders involving other purine enzymes.[37,38] We thus supplemented mild-ADSLd fibroblasts with adenine or guanine. Both

(F and G) (F) Western blotting analysis for AKT$^{pThr308}$ (including a higher exposure [h.e.]), AKT, ERK1/2$^{pThr202/Tyr204}$, and ERK1/2 in patients' fibroblasts after 10 min or 20 min of 70 nM insulin treatment. Densitometry analyses of AKT$^{pThr308}$ normalized against AKT and ERK1/2$^{pThr202/Tyr204}$ normalized against ERK1/2 following 20 min (20′) of insulin stimulation are also shown in (G). Values are mean ± SEM ($n \geq 3$).
(H and I) (H) Western blotting analysis for ERK1/2$^{pThr202/Tyr204}$ and ERK1/2 in patients' fibroblasts after 10 min or 20 min of 20 ng/μL EGF treatment. Densitometry analyses of ERK1/2$^{pThr202/Tyr204}$ normalized against ERK1/2 after 20 min (20′) of EGF treatment is also shown in (I). Values are mean ± SEM ($n = 5$).
Statistical analyses were performed using one-way ANOVA with Dunnett's multiple comparisons test or Friedman test with Dunn's multiple comparisons test. *$p < 0.05$, **$p < 0.01$, ***$p < 0.001$, and ****$p < 0.0001$.

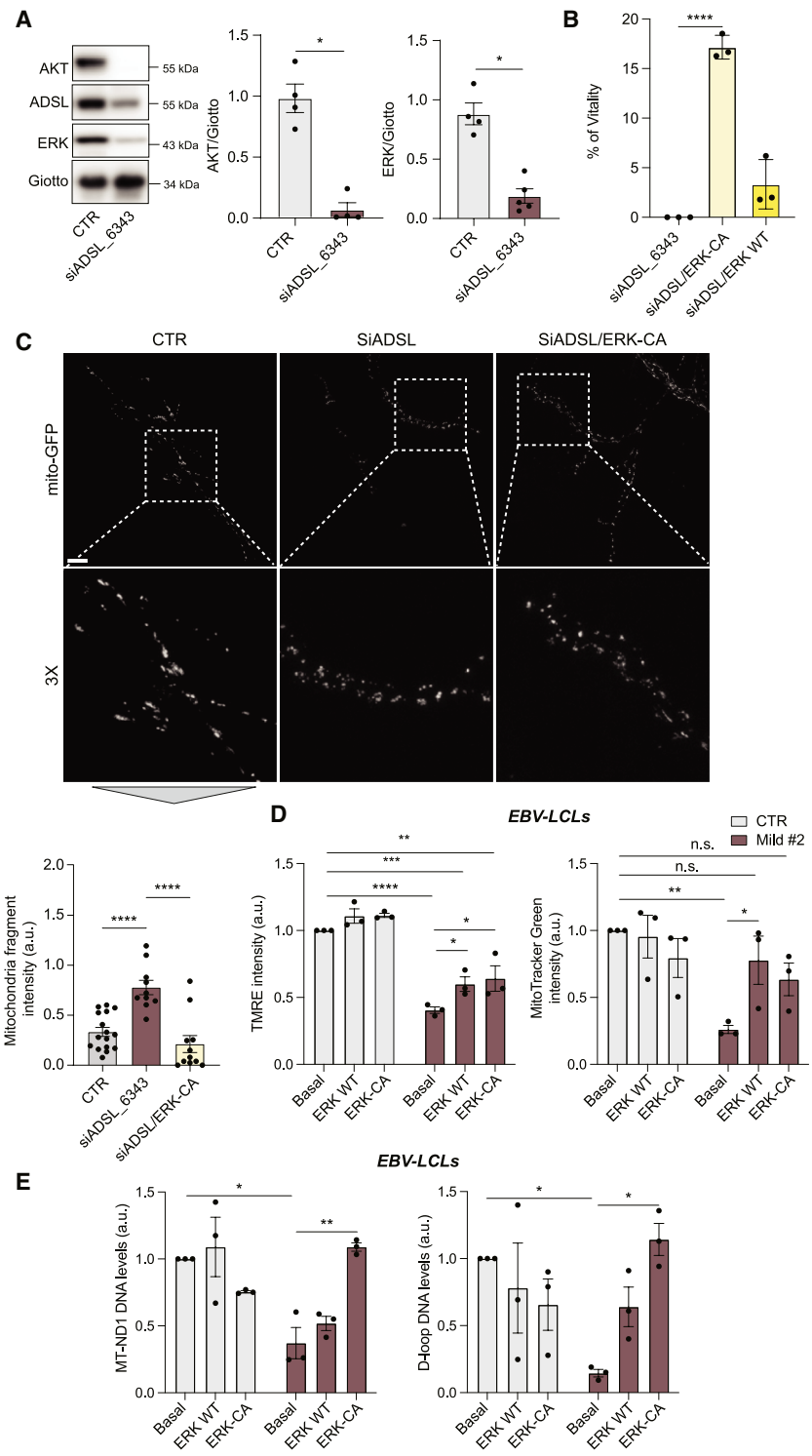


**Figure 6. ERK overexpression mitigates mitochondrial and viability defects associated with ADSLd in *Drosophila* and EBV-LCL models**

(A) Western blotting analysis for AKT, ADSL, and ERK in *Drosophila* larvae in which ADSL was downregulated in the muscles. Densitometry analysis of AKT, ADSL, and ERK normalized against Giotto is also shown (right). Values are mean ± SEM ($n \geq 4$).

(B) Viability assay of flies expressing ADSL RNAi under Mef2-GAL4 driver, together with wild-type ERK (UAS-ERK WT) or constitutively active ERK (UAS-ERK-CA). Viability was calculated as the percentage of adult flies carrying the Mef2-GAL4 and UAS constructs relative to the total number of progeny from each cross. Values are mean ± SEM from three independent biological replicates.

(C) Immunofluorescence analysis of the mitochondrial network of larval motoneurons expressing ADSL RNAi and ERK-CA and revealed by mito-GFP (white). Scale bar, 10 μm. The measure of mitochondrial fragmentation is also shown (bottom). Values are mean ± SEM ($n \geq 10$).

(D) Mitochondrial membrane potential was evaluated by TMRE staining (left), and mitochondrial mass was assessed by MitoTracker Green staining (right), followed by flow cytometry analysis in EBV-LCLs derived from control and mild #2 ADSLd cells. Cells were transduced to overexpress either wild-type ERK (ERK-WT) or constitutively active ERK (ERK-CA). Values are mean ± SEM ($n = 3$).

(E) Relative mtDNA content was assessed by measuring the copy number of *MT-ND1* gene and D loop region using qPCR in control and mild #2 EBV-LCLs overexpressing either ERK-WT or constitutively active ERK (ERK-CA). Data are expressed relative to control fibroblasts and reported in arbitrary units (a.u.). Values are mean ± SEM ($n = 3$).

Statistical analyses were performed using one-way ANOVA with Dunnett's multiple comparisons test or two-way ANOVA with Dunnett's multiple comparisons test or Mann-Whitney test when two groups were compared. *$p < 0.05$, **$p < 0.01$, ***$p < 0.001$, and ****$p < 0.0001$.

purines significantly ameliorated mitochondrial fragmentation, as shown by reduced mitochondrial circularity (Figures 7D and S7D), with no detectable effects in control cells. To determine whether morphological improvements correlated with functional recovery, we performed Seahorse assay. Remarkably, both adenine and guanine significantly enhanced mitochondrial respiration in mild patient-derived ADSLd fibroblasts (Figures 7E and 7F), as confirmed also by tetramethylrhodamine ethyl ester (TMRE) analysis (Figure S7E). In fibroblast control cells, guanine and (to a lesser extent) adenine elicited similar effects (Figures 7E and 7F). Furthermore, in ADSLd fibroblasts, both bases promoted a shift toward OXPHOS, accompanied by a compensatory reduction in glycolytic ATP production (Figure 7G). In control cells, a comparable metabolic shift was observed only in response to guanine. We also measured mitochondrial mass and quantified mtDNA copy number under the same conditions.

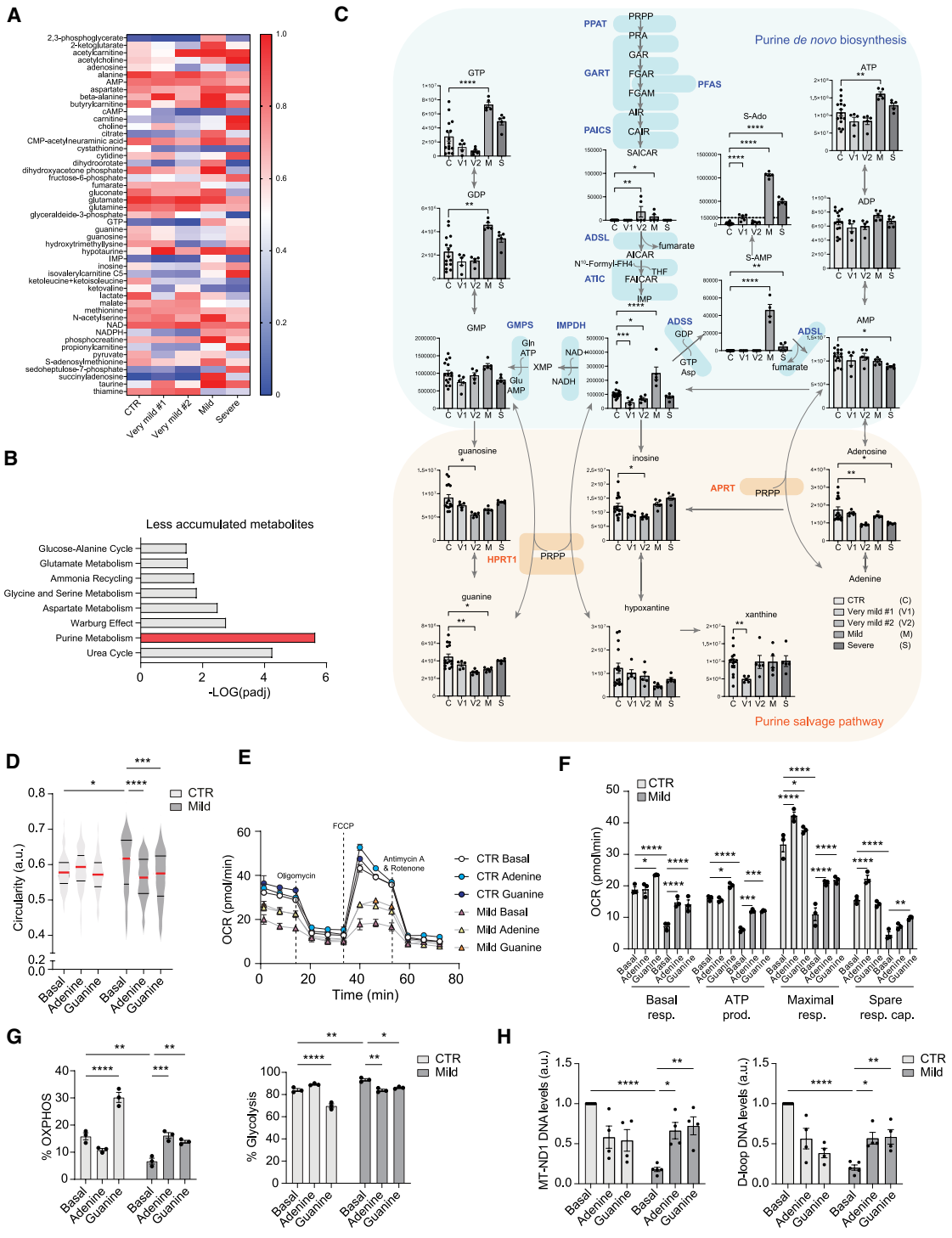


**Figure 7. Purine supplementation rescues mitochondrial defects in ADSLd fibroblasts**

(A) Heatmap displaying the relative abundance of metabolites emerged to be significantly altered in at least one of the patients. Metabolite concentrations were quantified by liquid chromatography-tandem mass spectrometry (LC-MS/MS) ($n \geq 3$).

(B) Metabolite set enrichment analysis (MSEA) of less-accumulated metabolites resulting from the metabolomic analysis.

(C) Relative abundance of purine pathway intermediates in the very Mild #1 (V1), very Mild #2 (V2), mild (M), and severe (S) patients compared to the control (C). Metabolite concentrations were quantified by LC-MS/MS. Values are mean ± SEM ($n = 5$).

*(legend continued on next page)*

We observed a notable increase in mitochondrial mass in mild-ADSLd fibroblasts following 48 h of adenine or guanine supplementation (Figure S7E). Additionally, mtDNA copy number was significantly elevated after 24 h of treatment with both bases (Figure 7H), further supporting the role of purines in restoring mitochondrial integrity and biogenesis in ADSLd cells.

We then extended these experiments to EBV-LCLs from ADSLd patients. Adenine and guanine consistently improved mitochondrial membrane potential and mass (Figure S7F). Given the metabolic link between purine and pyrimidine pathways,[39] we also tested uridine and cytidine. Unlike purines, pyrimidine supplementation did not affect mitochondrial mass or membrane potential (Figure S7G), underscoring the specific role of purines in restoring mitochondrial integrity in ADSLd cells.

## DISCUSSION

ADSLd is a rare autosomal disease that affects purine metabolism. The molecular mechanisms underlying pathogenesis are uncharacterized.[1] Several theories have been proposed, with the majority focusing on the toxicity of SAICAr and S-Ado accumulation and the absence of purine nucleotides and purine cycle.[1,5] Nevertheless, none of these explanations adequately elucidate all phenotypical features of ADSLd patients. Alteration of brain development and untreatable seizures, together with ataxic phenotypes, may not all be easily reconciled with a general reduction of nucleotides, which, however, might explain microcephaly and defects of neurodevelopment.[1] Accordingly, a deficiency in purine metabolism is expected to affect primarily more proliferating tissues. Indeed, by combining molecular biology techniques with *in vitro* and *in vivo* models, here we depicted a novel scenario in which variations on the *ADSL* gene affect mitochondrial homeostasis and the regulation of ERK2 and AKT kinases. Specifically, we used cells derived from six patients affected by all forms of ADSLd. This is a relevant number, especially when considering the rarity of the disease and the difficulty in acquiring samples from children with a severe systemic disorder.[1]

Current knowledge indicates that the severity of ADSLd clinical symptoms depends on the residual enzymatic activity of mutant ADSL and on its protein stability.[6,40,41] Further, it has also been hypothesized that ADSLd severity is affected not only by the intrinsic catalytic properties of the mutant proteins but also by their folding and ability to be assembled in a functional purinosome enzyme complex.[1,11] If, on the one hand, several *ADSL* mutations are known to produce enzymes that retain some residual enzymatic activity,[42] on the other hand, transcriptional regulation of the mutated *ADSL* gene has not been investigated. Here, we observed that, globally, *ADSL* mutations negatively affect protein expression by altering both mRNA and protein levels. We showed that the severity of disease correlates with the degree of ADSL downregulation, even though the *ADSL* gene promoter strongly resembles those found in housekeeping genes.[40] We also ruled out an increase in ADSL protein degradation and, notably, observed that the ADSL protein exhibited a robustly extended half-life. However, further studies need to be undertaken to address the correlation between pathogenic variants and the lower levels of ADSL in patients.

Although mutated ADSL exhibits aberrant transcriptional regulation, our data shed light on how the entire cellular metabolism is strongly altered in ADSLd-patient-derived cells and why the disease symptoms cannot be explained only by a defect in purine metabolism. Interestingly, we demonstrated through multiple lines of evidence that the impairments in mitochondrial activity and function are critical features of ADSLd. Interestingly, in addition to mitochondrial damage, ADSLd iPSCs showed increased cell death during neuronal differentiation, strongly suggesting that neurological and muscular abnormalities observed in ADSLd patients may be linked to mitochondrial dysfunction, as the nervous system and muscles rely heavily on mitochondria to meet their energy needs.[43]

From an evolutionary viewpoint, loss of ADSL function in yeast causes genomic instability and reduced viability, and in *Caenorhabditis elegans* results in slowed growth, infertility, reduction of lifespan, and locomotion defects.[44–46] Recently, it has been reported that ADSL depletion in chicken or zebrafish embryos affected neurogenesis and development, promoting higher DNA damage and microcephaly.[47]

Here, we demonstrated that *ADSL* silencing is lethal by RNAi-mediated downregulation of *ADSL* in different fly tissues, in line with previous observations in mice.[20] Emerging evidence from *Drosophila* and mammalian models highlights the importance of retrograde signaling from muscle to motor neurons in maintaining synaptic integrity at the NMJ.[48] Given this framework, we hypothesize that *ADSL* knockdown in muscle, through its impact on mitochondrial metabolism and energy homeostasis, may impair retrograde cues, ultimately leading to secondary synaptic dysfunction, including altered synapsin levels, and NMJ morphology.

Overall, our findings displayed the key role of ADSL in the nervous system and highlighted that alterations of ADSL in muscle

(D) Quantification of mitochondrial circularity on fibroblasts derived from control and mild ADSLd patients treated with 40 μM guanine or 40 μM adenine for 48 h. Mitochondrial circularity was quantified using ImageJ software. Values are mean ± SEM ($n$ = 3), with >60 cells analyzed per condition. In the violin plots, the red bars indicate median values, while the black bars (which may appear blue depending on rendering) represent the first and third quartiles.
(E) Oxygen-consumption rate (OCR) in control and mild ADSLd fibroblasts treated with 40 μM guanine or 40 μM adenine for 48 h, measured using the Seahorse XF Analyzer.
(F) Basal, ATP-coupled (ATP prod.), maximal respiration, and spare respiratory capacity of the cells in both control and patient-derived fibroblasts.
(G) ATP production rate from both mitochondrial and glycolytic pathways in control and mild ADSLd fibroblasts under the same treatment conditions. All values are mean ± SEM ($n$ = 3).
(H) Relative mtDNA content was assessed by measuring the copy number of *MT-ND1* gene and D loop region using qPCR in control and mild ADSLd fibroblasts treated with 40 μM guanine or 40 μM adenine for 24 h. Data are expressed relative to untreated control fibroblasts, normalized against genomic *β-ACTIN* levels and reported in arbitrary units (a.u.). Data represent mean ± SEM ($n$ = 4).
Statistical analyses were performed using one-way ANOVA with Dunnett's multiple comparisons test or two-way ANOVA with Dunnett's multiple comparisons test. $^{*}p < 0.05$, $^{**}p < 0.01$, $^{***}p < 0.001$, and $^{****}p < 0.0001$.

may also negatively impact motor neuron functions, suggesting that a possible connection exists. The maintenance of purine balance, encompassing the adenine pool, and the purine nucleotide cycle, where ADSL plays a significant role, hold paramount importance for the physiology and activity of skeletal muscle.[8,49,50] Therefore, it is imperative to ascertain whether ADSL has a discrete function in the regulation of mitochondrial respiration, beyond its participation in purine synthesis, or whether these two processes are interconnected.

Nucleotide synthesis is tightly biochemically regulated by allosteric feedback regulations and at the transcription level by the action of a collection of specific transcription factors.[22,51] Two major regulators of such factors are ERK1/2 and AKT, which play a central role in cell proliferation, survival, growth, and differentiation in the control of cell metabolism[23,25,52–54] and in the regulation of purine synthesis.[23,24,25] Importantly, when studying potential signaling pathways involved in ADSLd, we noted an overall reduction in activation of ERK2 and AKT in cells derived from patients with a more severe manifestation of the disease. This finding suggests that ADSL may modulate the AKT and ERK1/2 cascades and related cellular processes.[23,25,52–54]

The possibility of an association between ADSL and AKT/ERK2 regulation was supported by the altered activation of these kinases in ADSLd cells after glucose deprivation and reintroduction or upon insulin or EGF treatments, or in RNAi fly larvae implying that patient cells are somehow less responsive to external changes of physiological conditions or stimuli.

Overexpression of ERK-CA rescued lethality and mitochondrial defects in SiADSL flies and similarly restored mitochondrial activity, mass, and mtDNA copy number in ADSLd EBV-LCLs, highlighting a central role for ERK signaling in maintaining mitochondrial homeostasis downstream of ADSL. Future analysis is needed to understand the possible role of each *ADSL* mutation, to isolate the branch of the purine synthesis cascade that may be more involved in determining the form of ADSLd. Mass spectrometry analysis did not yield a distinct metabolic signature in ADSLd fibroblasts. However, an extensive accumulation of S-AMP and S-Ado was observed in mild and severe forms, indicating the presence of distinct compensatory mechanisms adopted by individual-form patients.

Finally, prompted by reduced guanine and adenosine levels in mild and severe ADSLd cells, and supported by previous evidence on adenine supplementation,[38] we improved mitochondrial morphology, activity, and mtDNA copy number in ADSLd fibroblasts and EBV-LCLs treated with guanine or adenine. These findings further support a functional link between purine metabolism and mitochondrial homeostasis.

In conclusion, this multi-model study of ADSLd provides an interpretation of the symptoms observed in patients by uncovering a novel link between ADSL, mitochondria, and the AKT/ERK pathways. The comprehension of the nature and regulation of this interconnection will contribute to revealing the molecular mechanisms governing ADSLd pathogenesis and, possibly, pave the way for new potential therapeutic strategies that might be based on mitochondrial boosting through nucleotides supplementation and/or attenuation of AKT/ERK2 dysfunctions.

### Limitations of the study

Our research confirms that ADSL deficiency, especially in severe forms, consistently leads to mitochondrial dysfunction and impaired ERK2/AKT signaling across various models. However, due to the rarity of the disease, we had limited patient-derived cell lines. Future studies will need a larger patient cohort to fully understand the range of clinical presentations and the role of ADSL in mitochondrial health.

## RESOURCE AVAILABILITY

### Lead contact

Further information and requests for materials should be directed to and will be fulfilled by the lead contact, Francesco Cecconi (francesco.cecconi@unicatt.it).

### Materials availability

This study did not generate new unique reagents.

### Data and code availability

- The metabolomic data from this publication was deposited to the NIH Common Fund's National Metabolomics Data Repository (NMDR) website, the Metabolomics Workbench, https://www.metabolomicsworkbench.org (project ID PR002082). All the relevant data supporting the main findings of the present study are available throughout the article and its supplemental information files or from the lead contact upon reasonable request.
- This paper does not report original code.
- Any additional information required to reanalyze the data reported in this paper is available from the lead contact upon request.

## ACKNOWLEDGMENTS

We are incredibly grateful to Benedetta Contardi for putting us in contact with many patients and for her enduring support. This work was supported, in part, by Telethon (grant GGP20109); the research also was funded by (1) the PNRR project "Adenylosuccinate lyase deficiency, purine metabolism disorders and mitochondrial homeostasis: unveiling novel mechanisms to design therapeutic opportunities," project ID: PNRR-MR1-2022-12376821, funded by the European Union – Next Generation EU - NRRP M6C2 - Investment 2.1 Enhancement and strengthening of biomedical research in the NHS and (2) the Italian Ministry of University and Research (MUR) under the National Recovery and Resilience Plan (PNRR), Mission 4 "Education and Research" – Component 2 "From Research to Enterprise" – Investment 1.3, through the project "Innovative models of brain diseases: a multiscale approach for the characterization of genetic and metabolic defects" (MEMENTO), within the Extended Partnership MNESYS (PE00000006_1), Spoke 3, University of Naples Federico II. Last, the work was also funded by EU funding within the MUR PNRR "National Center for Gene Therapy and Drugs based on RNA Technology" (project no. CN00000041 CN3 RNA), the Italian Ministry of Health (5 × 1000_2019, Current Research Funds, RCR-2022-23682289, and PNRR-MR1-2022-12376811), and #NEXTGENERATIONEU (NGEU). We express our gratitude to the laboratory led by Marie Zikánová for generously providing us with the ADSLd severe and the fatal neonatal primary fibroblasts.

## AUTHOR CONTRIBUTIONS

M.B. and F. Cecconi conceived the idea, developed the theory, and, together with B.T., designed the work plan and wrote the paper. A.B. and M.T. supervised and supported this work in addition to providing key intellectual advice. C.V. contributed to EBV cells analysis. C.C. and M.T. conceived the experiments related to the iPSC models. C.C. and F.C. generated the iPSC lines, performed their functional characterization, and analyzed the data. G.C., C. Carsetti and F. Cipressa generated, maintained, and analyzed *Drosophila melanogaster* flies. E.B., A.M., and C.F. performed biochemical analyses

and experiments on ADSLd cell lines. I.S. and A.F. performed Seahorse experiments and analyses. C.F. and M.Y. performed metabolomic analysis. R.D.C., E.D.P., and A.B. performed bioinformatic analyses. S.M. and E.Z. performed TEM experiments. S.R., E.D.P., and M.M. contributed to the drafting of the manuscript and figures. T.R. and R.C. contributed to the generation and storage of the primary fibroblasts. G.W. contributed to EBV cell line generation.

## DECLARATION OF INTERESTS

The authors declare no competing interests.

## STAR★METHODS

Detailed methods are provided in the online version of this paper and include the following:

- KEY RESOURCES TABLE
- EXPERIMENTAL MODEL AND STUDY PARTICIPANT DETAILS
  - Cell culture
  - Generation of ADSL patient-specific iPSCs
  - Fly lines
- METHOD DETAILS
  - Cell treatments
  - Transfections
  - Western blotting (WB)
  - Antibodies
  - Mitochondrial mass and transmembrane potential analysis
  - Oxygen consumption measurements
  - Immunofluorescence and confocal analysis
  - Analysis of mitochondrial network distribution
  - Positivity to alkaline phosphatase test
  - Immunofluorescence analysis to test pluripotency
  - DNA sequencing to confirm the mutations following reprogramming
  - Karyotype check following reprogramming
  - Trilineage differentiation potential
  - JC-1 staining
  - Motor neurons differentiation
  - Morphometric analysis using incucyte SX5 live cell analysis software
  - TUNEL assay
  - Analysis of cell viability and apoptosis in iPSCs
  - Analysis of mitochondrial network distribution in iPSCs
  - Metabolite extraction from cells
  - pHILIC LC-MS method
  - Real-Time PCR
  - Mitochondrial DNA (mtDNA) copy number quantification
  - GeneBridge analysis
  - Climbing assay
- *DROSOPHILA* EYE AREA QUANTIFICATION
  - Neuromuscular junction (NMJ) morphology analysis in Drosophila larvae
  - β-Galactosidase assay
  - Electron microscopy analysis
- QUANTIFICATION AND STATISTICAL ANALYSIS

## SUPPLEMENTAL INFORMATION

Supplemental information can be found online at https://doi.org/10.1016/j.celrep.2025.116230.

Received: October 24, 2024
Revised: May 27, 2025
Accepted: August 11, 2025
Published: September 5, 2025

## REFERENCES

1. Jurecka, A., Zikanova, M., Kmoch, S., and Tylki-Szymańska, A. (2015). Adenylosuccinate lyase deficiency. J. Inherit. Metab. Dis. *38*, 231–242. https://doi.org/10.1007/s10545-014-9755-y.
2. Jaeken, J., and Van den Berghe, G. (1984). An infantile autistic syndrome characterised by the presence of succinylpurines in body fluids. Lancet *2*, 1058–1061. https://doi.org/10.1016/S0140-6736(84)91505-8.
3. Salerno, C., D'Eufemia, P., Finocchiaro, R., Celli, M., Spalice, A., Iannetti, P., Crifò, C., and Giardini, O. (1999). Effect of D-ribose on purine synthesis and neurological symptoms in a patient with adenylosuccinase deficiency. Biochim. Biophys. Acta *1453*, 135–140. https://doi.org/10.1016/S0925-4439(98)00093-3.
4. De Volder, A.G., Jaeken, J., Van den Berghe, G., Bol, A., Michel, C., Cogneau, M., and Goffinet, A.M. (1988). Regional brain glucose utilization in adenylosuccinase-deficient patients measured by positron emission tomography. Pediatr. Res. *24*, 238–242. https://doi.org/10.1203/00006450-198808000-00020.
5. Spiegel, E.K., Colman, R.F., and Patterson, D. (2006). Adenylosuccinate lyase deficiency. Mol. Genet. Metab. *89*, 19–31. https://doi.org/10.1016/j.ymgme.2006.04.018.
6. Ray, S.P., Duval, N., Wilkinson, T.G., Shaheen, S.E., Ghosh, K., and Patterson, D. (2013). Inherent properties of adenylosuccinate lyase could explain S-Ado/SAICAr ratio due to homozygous R426H and R303C mutations. Biochim. Biophys. Acta *1834*, 1545–1553. https://doi.org/10.1016/j.bbapap.2013.05.013.
7. Sabina, R.L., Swain, J.L., Patten, B.M., Ashizawa, T., O'Brien, W.E., and Holmes, E.W. (1980). Disruption of the purine nucleotide cycle. A potential explanation for muscle dysfunction in myoadenylate deaminase deficiency. J. Clin. Investig. *66*, 1419–1423. https://doi.org/10.1172/JCI109995.
8. Van den Berghe, G., Bontemps, F., Vincent, M.F., and Van den Bergh, F. (1992). The purine nucleotide cycle and its molecular defects. Prog. Neurobiol. *39*, 547–561. https://doi.org/10.1016/0301-0082(92)90006-Z.
9. Ferreira, C.R. (2017). Prevalence of adenylosuccinate lyase deficiency based on aggregated exome data. Mol. Genet. Metab. Rep. *10*, 81–82. https://doi.org/10.1016/j.ymgmr.2016.12.009.
10. Macchiaiolo, M., Buonuomo, P.S., Mastrogiorgio, G., Bordi, M., Testa, B., Weber, G., Bellacchio, E., Tartaglia, M., Cecconi, F., and Bartuli, A. (2020). Very mild isolated intellectual disability caused by adenylosuccinate lyase deficiency: a new phenotype. Mol. Genet. Metab. Rep. *23*, 100592. https://doi.org/10.1016/j.ymgmr.2020.100592.
11. Baresova, V., Skopova, V., Sikora, J., Patterson, D., Sovova, J., Zikanova, M., and Kmoch, S. (2012). Mutations of ATIC and ADSL affect purinosome assembly in cultured skin fibroblasts from patients with AICA-ribosiduria and ADSL deficiency. Hum. Mol. Genet. *21*, 1534–1543. https://doi.org/10.1093/hmg/ddr591.
12. Pedley, A.M., and Benkovic, S.J. (2017). A New View into the Regulation of Purine Metabolism: The Purinosome. Trends Biochem. Sci. *42*, 141–154. https://doi.org/10.1016/J.TIBS.2016.09.009.
13. Mastrogiorgio, G., Macchiaiolo, M., Buonuomo, P.S., Bellacchio, E., Bordi, M., Vecchio, D., Brown, K.P., Watson, N.K., Contardi, B., Cecconi, F., et al. (2021). Clinical and molecular characterization of patients with adenylosuccinate lyase deficiency. Orphanet J. Rare Dis. *16*, 112. https://doi.org/10.1186/s13023-021-01731-6.
14. Huss, M., Ingenhorst, G., König, S., Gaßel, M., Dröse, S., Zeeck, A., Altendorf, K., and Wieczorek, H. (2002). Concanamycin A, the specific inhibitor of V-ATPases, binds to the VO subunit c. J. Biol. Chem. *277*, 40544–40548. https://doi.org/10.1074/jbc.M207345200.
15. Li, H., Rukina, D., David, F.P.A., Li, T.Y., Oh, C.M., Gao, A.W., Katsyuba, E., Bou Sleiman, M., Komljenovic, A., Huang, Q., et al. (2019). Identifying gene function and module connections by the integration of multispecies expression compendia. Genome Res *29*, 2034–2045. https://doi.org/10.1101/gr.251983.119.

16. Jiang, T., Sánchez-Rivera, F.J., Soto-Feliciano, Y.M., Yang, Q., Song, C. Q., Bhuatkar, A., Haynes, C.M., Hemann, M.T., and Xue, W. (2021). Targeting the De Novo Purine Synthesis Pathway Through Adenylosuccinate Lyase Depletion Impairs Liver Cancer Growth by Perturbing Mitochondrial Function. Hepatology *74*, 233–247. https://doi.org/10.1002/HEP.31685.

17. Zheng, X., Boyer, L., Jin, M., Mertens, J., Kim, Y., Ma, L., Ma, L., Hamm, M., Gage, F.H., and Hunter, T. (2016). Metabolic reprogramming during neuronal differentiation from aerobic glycolysis to neuronal oxidative phosphorylation. eLife *5*, e13374. https://doi.org/10.7554/ELIFE.13374.

18. Sheng, Z.H., and Cai, Q. (2012). Mitochondrial transport in neurons: impact on synaptic homeostasis and neurodegeneration. Nat. Rev. Neurosci. *13*, 77–93. https://doi.org/10.1038/NRN3156.

19. Hu, Y., Comjean, A., Rodiger, J., Liu, Y., Gao, Y., Chung, V., Zirin, J., Perrimon, N., and Mohr, S.E. (2021). FlyRNAi.org-the database of the Drosophila RNAi screening center and transgenic RNAi project: 2021 update. Nucleic Acids Res. *49*, D908–D915. https://doi.org/10.1093/nar/gkaa936.

20. Dickinson, M.E., Flenniken, A.M., Ji, X., Teboul, L., Wong, M.D., White, J. K., Meehan, T.F., Weninger, W.J., Westerberg, H., Adissu, H., et al. (2016). High-throughput discovery of novel developmental phenotypes. Nature *537*, 508–514. https://doi.org/10.1038/nature19356.

21. Vasin, A., Zueva, L., Torrez, C., Volfson, D., Littleton, J.T., and Bykhovskaia, M. (2014). Synapsin Regulates Activity-Dependent Outgrowth of Synaptic Boutons at the Drosophila Neuromuscular Junction. J. Neurosci. *34*, 10554–10563. https://doi.org/10.1523/JNEUROSCI.5074-13.2014.

22. Lane, A.N., and Fan, T.W.M. (2015). Regulation of mammalian nucleotide metabolism and biosynthesis. Nucleic Acids Res. *43*, 2466–2485. https://doi.org/10.1093/nar/gkv047.

23. Hoxhaj, G., and Manning, B.D. (2020). The PI3K–AKT network at the interface of oncogenic signalling and cancer metabolism. Nat. Rev. Cancer *20*, 74–88. https://doi.org/10.1038/s41568-019-0216-7.

24. Saha, A., Connelly, S., Jiang, J., Zhuang, S., Amador, D.T., Phan, T., Pilz, R.B., and Boss, G.R. (2014). Akt phosphorylation and regulation of transketolase is a nodal point for amino acid control of purine synthesis. Mol. Cell *55*, 264–276. https://doi.org/10.1016/j.molcel.2014.05.028.

25. Lavoie, H., Gagnon, J., and Therrien, M. (2020). ERK signalling: a master regulator of cell behaviour, life and fate. Nat. Rev. Mol. Cell Biol. *21*, 607–632. https://doi.org/10.1038/s41580-020-0255-7.

26. Ali, E.S., Sahu, U., Villa, E., O'Hara, B.P., Gao, P., Beaudet, C., Wood, A. W., Asara, J.M., and Ben-Sahra, I. (2020). ERK2 Phosphorylates PFAS to Mediate Posttranslational Control of De Novo Purine Synthesis. Mol. Cell *78*, 1178–1191.e6. https://doi.org/10.1016/j.molcel.2020.05.001.

27. Pareek, V., Pedley, A.M., and Benkovic, S.J. (2021). Human de novo purine biosynthesis. Crit. Rev. Biochem. Mol. Biol. *56*, 1–16. https://doi.org/10.1080/10409238.2020.1832438.

28. Monick, M.M., Powers, L.S., Barrett, C.W., Hinde, S., Ashare, A., Groskreutz, D.J., Nyunoya, T., Coleman, M., Spitz, D.R., and Hunninghake, G.W. (2008). Constitutive ERK MAP Kinase Activity Regulates Macrophage ATP Production and Mitochondrial Integrity. J. Immunol. *180*, 7485–7496. https://doi.org/10.4049/JIMMUNOL.180.11.7485.

29. Prieto, J., León, M., Ponsoda, X., Sendra, R., Bort, R., Ferrer-Lorente, R., Raya, A., López-Garciá, C., and Torres, J. (2016). Early ERK1/2 activation promotes DRP1-dependent mitochondrial fission necessary for cell reprogramming. Nat. Commun. *7*, 1–13. https://doi.org/10.1038/ncomms11124.

30. Deng, W., Leu, H.B., Chen, Y., Chen, Y.H., Epperson, C.M., Juang, C., and Wang, P.H. (2014). Protein kinase B (PKB/AKT1) formed signaling complexes with mitochondrial proteins and prevented glycolytic energy dysfunction in cultured cardiomyocytes during ischemia-reperfusion injury. Endocrinology *155*, 1618–1628. https://doi.org/10.1210/EN.2013-1817.

31. Yang, J.Y., Deng, W., Chen, Y., Fan, W., Baldwin, K.M., Jope, R.S., Wallace, D.C., and Wang, P.H. (2013). Impaired translocation and activation of mitochondrial Akt1 mitigated mitochondrial oxidative phosphorylation Complex V activity in diabetic myocardium. J. Mol. Cell. Cardiol. *59*, 167–175. https://doi.org/10.1016/J.YJMCC.2013.02.016.

32. Shin, S., Buel, G.R., Wolgamott, L., Plas, D.R., Asara, J.M., Blenis, J., and Yoon, S.O. (2015). ERK2 Mediates Metabolic Stress Response to Regulate Cell Fate. Mol. Cell *59*, 382–398. https://doi.org/10.1016/J.MOLCEL.2015.06.020.

33. Gao, M., Liang, J., Lu, Y., Guo, H., German, P., Bai, S., Jonasch, E., Yang, X., Mills, G.B., and Ding, Z. (2014). Site-specific activation of AKT protects cells from death induced by glucose deprivation. Oncogene *33*, 745–755. https://doi.org/10.1038/onc.2013.2.

34. Huang, Z., Xie, N., Illes, P., Di Virgilio, F., Ulrich, H., Semyanov, A., Verkhratsky, A., Sperlagh, B., Yu, S.G., Huang, C., and Tang, Y. (2021). From purines to purinergic signalling: molecular functions and human diseases. Signal Transduct. Target. Ther. *6*, 162. https://doi.org/10.1038/s41392-021-00553-z.

35. Abdullah, M.O., Zeng, R.X., Margerum, C.L., Papadopoli, D., Monnin, C., Punter, K.B., Chu, C., Al-Rofaidi, M., Al-Tannak, N.F., Berardi, D., et al. (2022). Mitochondrial hyperfusion via metabolic sensing of regulatory amino acids. Cell Rep. *40*, 111198. https://doi.org/10.1016/j.celrep.2022.111198.

36. Lew, S.Y., Mohd Hisam, N.S., Phang, M.W.L., Syed Abdul Rahman, S.N., Poh, R.Y.Y., Lim, S.H., Kamaruzzaman, M.A., Chau, S.C., Tsui, K.C., Lim, L.W., and Wong, K.H. (2023). Adenosine Improves Mitochondrial Function and Biogenesis in Friedreich's Ataxia Fibroblasts Following L-Buthionine Sulfoximine-Induced Oxidative Stress. Biology *12*, 559. https://doi.org/10.3390/BIOLOGY12040559.

37. Baresova, V., Skopova, V., Souckova, O., Krijt, M., Kmoch, S., and Zikanova, M. (2018). Study of purinosome assembly in cell-based model systems with de novo purine synthesis and salvage pathway deficiencies. PLoS One *13*, e0201432. https://doi.org/10.1371/journal.pone.0201432.

38. Mazzarino, R.C., Baresova, V., Zikánová, M., Duval, N., Wilkinson, T.G., Patterson, D., and Vacano, G.N. (2019). The CRISPR-Cas9 crADSL HeLa transcriptome: A first step in establishing a model for ADSL deficiency and SAICAR accumulation. Mol. Genet. Metab. Rep. *21*, 100512. https://doi.org/10.1016/j.ymgmr.2019.100512.

39. Mullen, N.J., and Singh, P.K. (2023). Nucleotide Metabolism: A Pan-Cancer Metabolic Dependency (Preprint at Nature Research). https://doi.org/10.1038/s41568-023-00557-7.

40. Kmoch, S., Hartmannová, H., Stibůrková, B., Krijt, J., Zikánová, M., and Sebesta, I. (2000). Human adenylosuccinate lyase (ADSL), cloning and characterization of full-length cDNA and its isoform, gene structure and molecular basis for ADSL deficiency in six patients. Hum. Mol. Genet. *9*, 1501–1513. https://doi.org/10.1093/hmg/9.10.1501.

41. Zikanova, M., Skopova, V., Hnizda, A., Krijt, J., and Kmoch, S. (2010). Biochemical and structural analysis of 14 mutant ADSL enzyme complexes and correlation to phenotypic heterogeneity of adenylosuccinate lyase deficiency. Hum. Mutat. *31*, 445–455. https://doi.org/10.1002/humu.21212.

42. Van den Bergh, F., Vincent, M.F., Jaeken, J., and Van den Berghe, G. (1993). Functional studies in fibroblasts of adenylosuccinase-deficient children. J. Inherit. Metab. Dis. *16*, 425–434. https://doi.org/10.1007/BF00710293.

43. Zink, A., Priller, J., and Prigione, A. (2018). Pluripotent Stem Cells for Uncovering the Role of Mitochondria in Human Brain Function and Dysfunction. J. Mol. Biol. *430*, 891–903. https://doi.org/10.1016/j.jmb.2018.02.005.

44. Marsac, R., Pinson, B., Saint-Marc, C., Olmedo, M., Artal-Sanz, M., Daignan-Fornier, B., and Gomes, J.E. (2019). Purine Homeostasis Is Necessary for Developmental Timing, Germline Maintenance and Muscle Integrity in Caenorhabditis elegans. Genetics *211*, 1297–1313. https://doi.org/10.1534/GENETICS.118.301062.

45. Chen, P., Wang, D., Chen, H., Zhou, Z., and He, X. (2016). The nonessentiality of essential genes in yeast provides therapeutic insights into a human disease. Genome Res. *26*, 1355–1362. https://doi.org/10.1101/GR.205955.116.

46. Daignan-Fornier, B., and Pinson, B. (2019). Yeast to study human purine metabolism diseases. Cells *8*, 67. https://doi.org/10.3390/cells8010067.

47. Dutto, I., Gerhards, J., Herrera, A., Souckova, O., Škopová, V., Smak, J.A., Junza, A., Yanes, O., Boeckx, C., Burkhalter, M.D., et al. (2022). Pathway-specific effects of ADSL deficiency on neurodevelopment. eLife *11*, e70518. https://doi.org/10.7554/ELIFE.70518.

48. Harrell, E.R., Pimentel, D., and Miesenböck, G. (2021). Changes in presynaptic gene expression during homeostatic compensation at a central synapse. J. Neurosci. *41*, 3054–3067. https://doi.org/10.1523/JNEUROSCI.2979-20.2021.

49. Hoxhaj, G., Hughes-Hallett, J., Timson, R.C., Ilagan, E., Yuan, M., Asara, J.M., Ben-Sahra, I., and Manning, B.D. (2017). The mTORC1 Signaling Network Senses Changes in Cellular Purine Nucleotide Levels. Cell Rep. *21*, 1331–1346. https://doi.org/10.1016/j.celrep.2017.10.029.

50. Flanagan, W.F., Holmes, E.W., Sabina, R.L., and Swain, J.L. (1986). Importance of purine nucleotide cycle to energy production in skeletal muscle. Am. J. Physiol. *251*, C795–C802. https://doi.org/10.1152/AJPCELL.1986.251.5.C795.

51. Liu, Y.C., Li, F., Handler, J., Huang, C.R.L., Xiang, Y., Neretti, N., Sedivy, J.M., Zeller, K.I., and Dang, C.V. (2008). Global regulation of nucleotide biosynthetic genes by c-myc. PLoS One *3*, e2722. https://doi.org/10.1371/journal.pone.0002722.

52. Zhu, J., Blenis, J., and Yuan, J. (2008). Activation of PI3K/Akt and MAPK pathways regulates Myc-mediated transcription by phosphorylating and promoting the degradation of Mad1. Proc. Natl. Acad. Sci. USA *105*, 6584–6589. https://doi.org/10.1073/pnas.0802785105.

53. Marampon, F., Ciccarelli, C., and Zani, B.M. (2006). Down-regulation of c-Myc following MEK/ERK inhibition halts the expression of malignant phenotype in rhabdomyosarcoma and in non muscle-derived human tumors. Mol. Cancer *5*, 31. https://doi.org/10.1186/1476-4598-5-31.

54. Albihn, A., Johnsen, J.I., and Henriksson, M.A. (2010). MYC in Oncogenesis and as a Target for Cancer Therapies. Adv. Cancer Res. *107*, 163–224. https://doi.org/10.1016/S0065-230X(10)07006-5.

55. Caruana, I., Weber, G., Ballard, B.C., Wood, M.S., Savoldo, B., and Dotti, G. (2015). K562-Derived Whole-Cell Vaccine Enhances Antitumor Responses of CAR-Redirected Virus-Specific Cytotoxic T Lymphocytes In Vivo. Clin. Cancer Res. *21*, 2952–2962. https://doi.org/10.1158/1078-0432.CCR-14-2998.

56. Giansanti, M.G., Bonaccorsi, S., Kurek, R., Farkas, R.M., Dimitri, P., Fuller, M.T., and Gatti, M. (2006). The class I PITP giotto is required for Drosophila cytokinesis. Curr. Biol. *16*, 195–201. https://doi.org/10.1016/j.cub.2005.12.011.

57. Corti, S., Nizzardo, M., Simone, C., Falcone, M., Nardini, M., Ronchi, D., Donadoni, C., Salani, S., Riboldi, G., Magri, F., et al. (2012). Genetic correction of human induced pluripotent stem cells from patients with spinal muscular atrophy. Sci. Transl. Med. *4*, 165ra162. https://doi.org/10.1126/SCITRANSLMED.3004108.

58. Madabattula, S.T., Strautman, J.C., Bysice, A.M., O'Sullivan, J.A., Androschuk, A., Rosenfelt, C., Doucet, K., Rouleau, G., and Bolduc, F. (2015). Quantitative Analysis of Climbing Defects in a Drosophila Model of Neurodegenerative Disorders. J. Vis. Exp. *2015*, e52741. https://doi.org/10.3791/52741.

## STAR★METHODS

### KEY RESOURCES TABLE

| REAGENT or RESOURCE | SOURCE | IDENTIFIER |
|---|---|---|
| Antibodies | | |
| *p*-Akt (Thr308) | Cell Signaling Technology | Cat# 9275; RRID:AB_329828 |
| AKT | Cell Signaling Technology | Cat# 9272; RRID:AB_329827 |
| *p*-ERK1/2 (Thr202/Tyr204) | Cell Signaling Technology | Cat# 9101; RRID:AB_331646 |
| ERK1/2 | Cell Signaling Technology | Cat# 9102; RRID:AB_330744 |
| LC3B (D11) XP | Cell Signaling Technology | Cat# 3868; RRID:AB_2137707 |
| Cyclin B1 | Cell Signaling Technology | Cat# 4138; RRID:AB_2072132 |
| OPA1 | Cell Signaling Technology | Cat# 80471; RRID:AB_2734117 |
| *p*-DRP1 (Ser616) | Cell Signaling Technology | Cat# 3455; RRID:AB_2085352 |
| DRP1 | Cell Signaling Technology | Cat# 8570; RRID:AB_10950498 |
| ADSL | Santa Cruz Biotechnology | Cat# sc-365623; RRID:AB_10850305 |
| GAPDH | Santa Cruz Biotechnology | Cat# sc-32233; RRID:AB_627679 |
| HSP90α/β (F-8) | Santa Cruz Biotechnology | Cat# sc-13119; RRID:AB_675659 |
| TOM20 (F-10) | Santa Cruz Biotechnology | Cat# sc-17764; RRID:AB_628381 |
| UBIQUITIN | Santa Cruz Biotechnology | Cat# sc-8017; RRID:AB_628423 |
| MFN2 | Santa Cruz Biotechnology | Cat# sc-515647; RRID:AB_2811176 |
| ACTIN | Sigma-Aldrich | Cat# A2066; RRID:AB_476693 |
| Monoclonal ANTI-FLAG® M2 | Sigma-Aldrich | Cat# F1804; RRID:AB_262044 |
| OxPhos Human antibody cocktail | Thermo Fisher Scientific | Cat# 45-8099; RRID:AB_2533835 |
| Giotto | Kindly provided by M.G. Giansanti - CNR | RRID:AB_2892585 |
| SYN | Developmental Studies Hybridoma Bank | Cat# 3C11 (anti SYNORF1); RRID: AB_528479 |
| HRP (Peroxidase AffiniPure® Rabbit Anti-Human IgG (H + L)) | Jackson ImmunoResearch | Cat# 309-035-003; RRID: AB_2339647 |
| Discs large | Developmental Studies Hybridoma Bank | Cat# 4F3 anti-discs large; RRID: AB_528203 |
| MTC02 | Novus Biologicals | Cat# NB600-556; RRID:AB_10125201 |
| βIII-Tubulin | Sigma-Aldrich | Cat# T2200; RRID:AB_262133 |

(*Continued on next page*)

*Continued*

| REAGENT or RESOURCE | SOURCE | IDENTIFIER |
|---|---|---|
| Goat Anti-Rabbit IgG (H + L)-HRP Conjugate | Bio-Rad | Cat# 1706515; RRID:AB_11125142 |
| Goat Anti-Mouse IgG (H + L)-HRP Conjugate | Bio-Rad | Cat# 1706516; RRID:AB_2921252 |
| F(ab')2-Goat anti-Rabbit IgG (H + L) Cross-Adsorbed Secondary Antibody, Alexa Fluor™ 555 | Thermo Fisher Scientific | Cat# A-21430; RRID:AB_2535851 |
| F(ab')2-Goat anti-Rabbit IgG (H + L) Cross-Adsorbed Secondary Antibody, Alexa Fluor™ 488 | Thermo Fisher Scientific | Cat# A-11070; RRID:AB_2534114 |
| F(ab')2-Goat anti-Mouse IgG (H + L) Cross-Adsorbed Secondary Antibody, Alexa Fluor™ 488 | Thermo Fisher Scientific | Cat# A-11017; RRID:AB_2534084 |
| F(ab')2-Goat anti-Mouse IgG (H + L) Cross-Adsorbed Secondary Antibody, Alexa Fluor™ 555 | Thermo Fisher Scientific | Cat# A-21425; RRID:AB_2535846 |
| Rhodamine (TRITC) AffiniPure® Goat Anti-Rabbit IgG (H + L) | Jackson ImmunoResearch | Cat# 111-025-003; RRID:AB_2337926 |
| Rhodamine (TRITC) AffiniPure® Goat Anti-Mouse IgG (H + L) | Jackson ImmunoResearch | Cat# 115-025-146; RRID:AB_2338488 |
| OCT-4 | Thermo Fisher Scientific | Cat# MA5-14845; RRID:AB_10979606 |
| SOX-2 | Thermo Fisher Scientific | Cat# 14-9811-82; RRID:AB_11219471 |
| SSEA4 | Thermo Fisher Scientific | Cat# MA1-021; RRID:AB_2536687 |
| TRA1-60 | Santa Cruz Biotechnology | Cat# sc-21705; RRID:AB_628385 |
| SOX17 | Cell Signaling Technology | Cat# 81778; RRID:AB_2650582 |
| NCAM-L1 | Cell Signaling Technology | Cat# 89861; RRID:AB_2800145 |
| Brachyury | Cell Signaling Technology | Cat# 81694; RRID:AB_2799983 |
| **Chemicals, peptides, and recombinant proteins** | | |
| DMEM | EuroClone | Cat# ECB7501L |
| Fetal Bovine Serum (FBS) | Life Technologies (GIBCO) | Cat# 10270106 |
| Penicillin/streptomycin | EuroClone | Cat# ECB3001B |
| DMEM/F-12 | Life Technologies (GIBCO) | Cat# 11320033 |
| RPMI | EuroClone | Cat# ECM2001L |
| L-Glutamine | EuroClone | Cat# ECB3000D |
| Insulin | Sigma-Aldrich | Cat# I9278 |
| EGF | Sigma-Aldrich | Cat# E5036 |
| Chloroquine (CLQ) | Sigma-Aldrich | Cat# C6628 |
| Concanamycin A (ConA) | Sigma-Aldrich | Cat# C9705 |
| MG132 | Sigma-Aldrich | Cat# M7449 |
| Cycloheximide (CHX) | Sigma-Aldrich | Cat# 239765 |
| Dihydroethidium (DHE) | Thermo Fisher Scientific | Cat# D23107 |
| Adenine | Sigma-Aldrich | Cat# A9795 |
| Guanine | Sigma-Aldrich | Cat# G11950 |
| Cytidine | Sigma-Aldrich | Cat# C4654 |
| Uridine | Sigma-Aldrich | Cat# U3003 |

(*Continued on next page*)

*Continued*

| REAGENT or RESOURCE | SOURCE | IDENTIFIER |
|---|---|---|
| Phosphate-buffered saline (PBS) | EuroClone | Cat# ECB4053 |
| glucose-free DMEM | Thermo Fisher Scientific | Cat# 11966025 |
| TMRE | Thermo Fisher Scientific | Cat# T669 |
| JC-1 (5,5′,6,6′-tetrachloro-1,1′,3,3′-tetraethyl-imidacarbocyanine iodide) | Thermo Fisher Scientific | Cat# T3168 |
| MitoTracker™ Green FM | Thermo Fisher Scientific | Cat# M7514 |
| MitoTracker™ Red CMXRos | Thermo Fisher Scientific | Cat# M7512 |
| Lipofectamine™ RNAiMAX | Thermo Fisher Scientific | Cat# 13778075 |
| Protease inhibitor cocktail (PIC) | Sigma-Aldrich | Cat# P8340 |
| β-glycerophosphate | Sigma-Aldrich | Cat# G9422 |
| $Na_4VO_3$ | Sigma-Aldrich | Cat# S6508 |
| NaF | Sigma-Aldrich | Cat# 201154 |
| Oligomycin | Sigma-Aldrich | Cat# 75351 |
| FCCP (Carbonyl cyanide-4-(trifluoromethoxy) phenylhydrazone) | Sigma-Aldrich | Cat# SML2959 |
| Rotenone | Sigma-Aldrich | Cat# R8875 |
| Antimycin A | Sigma-Aldrich | Cat# A8674 |
| Fibronectin | Sigma-Aldrich | Cat# F2006 |
| Formaldehyde solution | Sigma-Aldrich | Cat# 252549 |
| Triton X-100 | Sigma-Aldrich | Cat# T8787 |
| Normal Goat Serum (NGS) | Thermo Fisher Scientific | Cat# 31872 |
| Hoechst | Thermo Fisher Scientific | Cat# H3570 |
| Fluoromount™ Aqueous Mounting Medium | Sigma-Aldrich | Cat# F4680 |
| VECTASHIELD® Antifade Mounting Medium with DAPI | Vector Laboratories | Cat# H-1200-10 |
| Matrigel-Matrix hESC-qualified | Corning | Cat# 354277 |
| mTeSR™1 | STEMCELL Technologies | Cat# 85850 |
| Ethylenediaminetetraacetic acid disodium salt dihydrate (EDTA) | Sigma-Aldrich | Cat# S-E1644 |
| Formaldehyde, methanol free | Thermo Fisher Scientific | Cat# 28908 |
| Glycerol | Sigma-Aldrich | Cat# G6279 |
| LC-MS grade Methanol | Thermo Fisher Scientific | Cat# 10284580 |
| LC-MS grade Acetonitrile | Thermo Fisher Scientific | Cat# 10001334 |
| Ultrapure water | Sigma-Aldrich | Cat# 270733 |
| Valine-d8 | CK isotopes | Cat# DLM-488 |
| M-MLV enzyme | Promega | Cat# C1101 |
| SYBR™ Green PCR Master Mix | Thermo Fisher Scientific | Cat# 4309155 |
| Epoxy-Resin | Sigma-Aldrich | Cat# 31190 |
| Rhodamine Phalloidin | Cytoskeleton, Inc. | Cat# PHDR1 |
| **Critical commercial assays** | | |
| Neon Transfection System | Thermo Fisher Scientific | Cat# MPK10025 |
| Folin-Lowry assay (DC Protein assay) | Bio-Rad® | Cat# 5000111 |
| Pierce™ BCA Protein Assay Kit | Thermo Fisher Scientific | Cat# 23225 |
| ECL | Merck Millipore | Cat# WPKLS0500 |
| Seahorse XF Cell Mito Stress Test Kit | Agilent | Cat# 103015-100 S |
| Seahorse XF Real-Time ATP Rate Assay Kit | Agilent | Cat# 103592-100 |
| Epi5 Episomal iPSC Reprogramming Kit | Invitrogen | Cat# A15960 |
| P2 Primary Cell 4D-Nucleofector® X Kit L | Lonza | Cat# V4XP2024 |
| Leukocyte Alkaline Phosphatase Kit | Sigma-Aldrich | Cat# 86R-1KT |

(*Continued on next page*)

*Continued*

| REAGENT or RESOURCE | SOURCE | IDENTIFIER |
|---|---|---|
| MagPurix Culture Cell DNA extraction kit | Zinexts Life Science | Cat# ZP02005 |
| KAPA2G Fast ReadyMix Kit | Sigma-Aldrich | Cat# S-KK5101 |
| hPSC Genetic Analysis Kit | STEMCELL Technologies | Cat# 07550 |
| STEMdiffTrilineage Differentiation Kit | STEMCELL Technologies | Cat# 05230 |
| DeadEnd™ Fluorometric TUNEL System | Promega | Cat# G3250 |
| QIAGEN DNeasy Blood and Tissue Kit | Qiagen | Cat# 69504 |
| ReliaPrep kit RNA Miniprep Systems | Promega | Cat# Z6011 |
| β-Galactosidase assay kit | Thermo Fisher Scientific | Cat# 75707 |
| **Deposited data** | | |
| Metabolomic data | NIH Common Fund's National Metabolomics Data Repository (NMDR) website, the Metabolomics Workbench | https://www.metabolomicsworkbench.org Project ID PR002082 |
| **Experimental models: Cell lines** | | |
| SH-SY5Y | ATCC | Cat# CRL-2266; RRID:CVCL_0019 |
| EBV-LCLs derived from patients (See Figure S1A for list of patients) | In-house made as reported in Caruana et al.[55] | N/A |
| Primary human fibroblasts derived from Wildtype, Very mild-form and Mild-form patients (See Figure S1A for list of patients) | Bambino Gesù Children's Hospital | N/A |
| Primary human fibroblasts derived from Severe-form and Fatal neonatal-form patients (See Figure S1A for list of patients) | Kindly provided by Zikánová Charles University in Prague | N/A |
| **Experimental models: Organisms/strains** | | |
| *Drosophila*: v6343 (w1118; P{GD1722}v6343) | Vienna Drosophila Resource Center | Cat# v6343 |
| *Drosophila*: v103823(P{KK108187}VIE-260B) | Vienna Drosophila Resource Center | Cat# v103823 |
| *Drosophila*: Act-GAL4((y[1] w[*]; P{w[+mC] = Act5C-GAL4}17bFO1/TM6B, Tb[1]) | Bloomington Drosophila Stock Center | Cat# 3954; RRID:BDSC_3954 |
| *Drosophila*: 69B-GAL4 ((w[*]; P{w[+mW.hs] = GawB}69B) | Bloomington Drosophila Stock Center | Cat# 1774; RRID:BDSC_1774 |
| *Drosophila*: Mef2-GAL4 ((w[*]; Kr[If-1]/CyO, P{w[+mC] = GAL4-Mef2.R}2, P{w[+mC] = UAS-mCD8.mRFP}2) | Bloomington Drosophila Stock Center | Cat# 26882; RRID:BDSC_26882 |
| *Drosophila*: D-42-GAL4((w[*]; P{w[+mW.hs] = GawB}D42) | Bloomington Drosophila Stock Center | Cat# 8816; RRID:BDSC_8816 |
| *Drosophila*: D-42-GAL4,mito-GFP ((w[1118]; P{w[+mW.hs] = GawB}D42, P{w[+mC] = UAS-mito-HA-GFP.AP}3 e[1]/TM6B, Tb[1]) | Bloomington Drosophila Stock Center | Cat# 42737; RRID:BDSC_42737 |
| *Drosophila*: ERKCA (y[1] w[*]; P{w[+mC] = UAS-rl[Sem].S}2ERK59CA) | Bloomington Drosophila Stock Center | Cat# 59006; RRID:BDSC_59006 |
| *Drosophila*: ERKWT(w[1118]; P{w[+mC] = UAS-rl.K}2A) | Bloomington Drosophila Stock Center | Cat# 36270; RRID:BDSC_36270 |
| **Oligonucleotides** | | |
| esiRNA targeting human ADSL | Sigma-Aldrich | Cat# EHU070001 |
| Stealth RNAi™ siRNA Negative Control | Thermo Fisher Scientific | Cat# 12935300 |
| *ADSL*-Primer-F: GGAGATGTGCTTCGTGTTTAG | This paper | N/A |
| *ADSL*-Primer-R: GTCGATGTTCTCCAGGTTTG | This paper | N/A |
| *HPRT1*-Primer-F: CTGAGGATTTGGAAAGGGTG | This paper | N/A |
| *HPRT1*-Primer-R: CAGAGGGCTACAATGTGATG | This paper | N/A |
| *COXII*-Primer-F: TGCCCGCCATCATCCTA | This paper | N/A |

(*Continued on next page*)

*Continued*

| REAGENT or RESOURCE | SOURCE | IDENTIFIER |
|---|---|---|
| *COXII*-Primer-R: TCGTCTGTTATGTAAAGGATGCGT | This paper | N/A |
| *ATP6*-Primer-F: ACACCCCTTATCCCCATACTAG | This paper | N/A |
| *ATP6*-Primer-R: ATGGTTGATATTGCTAGGGTGG | This paper | N/A |
| *ND3*-Primer-F: AGAAAAATCCACCCCTTACGGT | This paper | N/A |
| *ND3*-Primer-R: TGGAGAAAGGGACGCGG | This paper | N/A |
| *B2M*-Primer-F: CTCCGTGGCCTTAGCTGTG | This paper | N/A |
| *B2M*-Primer-R: TCTCTGGATGACGTGAG | This paper | N/A |
| *ACTB*-Primer-F: CCCCTGGCGGCCTAAGGACT | This paper | N/A |
| *ACTB*-Primer-R: ACATGCCGGAGCCGTTGTCG | This paper | N/A |
| *D-loop*-Primer-F: ACCACCCAAGTATTGACTCACC | This paper | N/A |
| *D-loop*-Primer-R: CCGTACAATATTCATGGTGGCT | This paper | N/A |
| *MT-ND1*-Primer-F: TTCTCCGATCCGTCCCTAACA | This paper | N/A |
| *MT-ND1*-Primer-R: GGTTGTCCTCCGATTCAGGTT | This paper | N/A |
| **Recombinant DNA** | | |
| p3xFlag-CMV7-Erk2 | Addgene | Cat# 39223; RRID:Addgene_39223 |
| p3xFlag-CMV7-Erk2-L73P-S151D | Ali et al.[26] | p3xFlag-CMV7-Erk2-L73P-S151D (ERK2-CA) |
| **Software and algorithms** | | |
| ImageJ | Schneider et al., 2012 | RRID: SCR_003070 |
| GraphPad Prism 9 | GraphPad Prism | https://www.graphpag.com/features RRID:SCR_002798 |
| Adobe Photoshop CS6 | Adobe Systems Inc. | https://helpx.adobe.com/it/creative-suite/kb/cs6-install-instructions.html |
| ZEN 3.1 Blue Edition software | Zeiss | https://www.zeiss.com/microscopy/en/products/software/zeiss-zen.html |
| LAS-X software | Leica Microsystems | https://www.leica-microsystems.com/it/prodotti/software-per-microscopi/p/leica-las-x-ls/ |
| Seahorse Wave Desktop Software version 2.6.3.5 | Wave | RRID:SCR_014526 |
| Incucyte® Neurotrack Analysis Software | Sartorius | https://www.sartorius.com/en/products/live-cell-imaging-analysis/live-cell-analysis-software/incucyte-neurotrack-analysis-software |
| Tracefinder 5.0 | Thermo Fisher Scientific | https://assets.thermofisher.com/TFS-Assets/CMD/manuals/man-xcali-97863-tracefinder-50-user-efs-manxcali97863-en.pdf |
| AccuCor algorithm | GitHub | https://github.com/lparsons/accucor |
| GeneBridge correlation analysis | Systems-Genetics | https://systems-genetics.org |
| **Other** | | |
| PVDF | Merck Millipore | Cat# IPVH00010 |
| Seahorse XFe96 Analyzer | Agilent | Cat# S7800A |
| Agilent Seahorse microplates | Agilent | Cat# 101085-004 |
| Zeiss Confocal microscope | Zeiss | Model: LSM 800 |
| Leica Confocal microscope | Leica Microsystems | Model: TCS-SP8X |
| Leica Confocal microscope | Leica Microsystems | Model: Stellaris |
| Zeiss Confocal microscope | Zeiss | Model: LSM 700 |
| 4D-Nucleofector® X Unit | Lonza | Cat# AAF-1003X |
| EVOS microscopy system | Thermo Fisher Scientific | |
| Leica Microscope | Leica Microsystems | Model: DM1000 |

(*Continued on next page*)

*Continued*

| REAGENT or RESOURCE | SOURCE | IDENTIFIER |
|---|---|---|
| Auto DNA Extraction MagPurix | Zinexts Life Science | Model: MagPurix 12s |
| Plasmid Sanger sequencer | Thermo Fisher Scientific | Model: SeqStudio Genetic Analyzer |
| Leica Microscope | Leica Microsystems | Model: DMi8 |
| Live-Cell Imaging and Analysis Instrument (Incucyte) | Sartorius | Model: Incucyte® SX5 |
| Matrigel 96-well plates | Merck | Cat# Z707910 |
| Flow Cytometer | BD Biosciences | Model: BD FACSVerse™ |
| Autosampler vials | Sigma-Aldrich | Cat# 29659-U |
| SeQuant® ZIC®-pHILIC 5μm polymer 150 x 2.1 mm | Merck | Cat# 150460 |
| Mass Spectrometer | Thermo Fisher Scientific | Model: Q Exactive™ Plus Hybrid Quadrupole-Orbitrap™ Mass Spectrometer |
| QuantStudio™ 3 Real-Time PCR System | Thermo Fisher Scientific | Cat# A28567 |
| Stereo microscope | Zeiss | Model: Stemi 508 |
| Ultrotome V Microtome System Lab | LKB Bromma | Model: LKB Bromma 2088 |
| Transmissione electron microscope | Fei Company | Model: Tecnai G2 |

## EXPERIMENTAL MODEL AND STUDY PARTICIPANT DETAILS

### Cell culture

The experiments were performed on the following cell lines: SH-SY5Y; EBV-LCLs (Epstein Barr Virus-transformed lymphoblastoid cell lines) derived from ADSLd patients as previously reported[55]; primary human fibroblasts derived from skin biopsies of ADSLd patients (from Bambino Gesù Children's Hospital and Charles University of Prague). Primary fibroblasts were cultured in DMEM (EuroClone #ECB7501L) supplemented with 10% FBS (Gibco Life Technologies #10270106) and 1% penicillin/streptomycin (EuroClone #ECB3001B). SH-SY5Y cells were cultured in DMEM/F-12 (Gibco Life Technologies #11320033) supplemented with the same compounds described above. EBV-LCLs were cultured in RPMI (EuroClone #ECM2001L) supplemented with 2 mM L-Glutamine (EuroClone #ECB3000D) and the same compounds described above. Cells were maintained in a humidified atmosphere containing 5% $CO_2$ at 37°C.

### Generation of ADSL patient-specific iPSCs

We generated iPSCs from skin fibroblasts of four patients carrying deleterious variants in *ADSL* gene c.78G>A (p.Met26Ile)/c.1187G>A (p.Arg396His), c.926G>A (p.Arg309His)/c.1191 + 5G>C, c.1277G>A (p.Arg426His)/c.340T>C (p.Tyr114His) and c.8C>T (p.Ala3Val)/c.1009C>T (p.Arg337Ter), reported in Figure S1A according to RefSeq NM_000026.4 and NP_000017.1). ADSL patient-specific fibroblasts were reprogrammed using non-integrating episomal vectors (Epi5 Episomal iPSC Reprogramming Kit, #A15960, Invitrogen, Waltham, USA). Specifically, fibroblasts from each patient were first cultured in Dulbecco's Modified Eagle Medium (DMEM, #D5671, Sigma Aldrich, St. Louis, USA) supplemented with 10% of Fetal Bovine Serum (FBS, #10082-147, Gibco, Waltham, USA) at 37°C, 5% $CO_2$. Differentiated cells were then reprogrammed by nucleofection using vectors containing the following five transcription factors OCT4, SOX2, LIN28, KLF4, and L-MYC and the Nucleofection kit P2 solution (#LOV4XP2024, Lonza, Basilea, Switzerland). 4D-Nucleofector System was employed for electroporation (Lonza, Basilea, Switzerland) and transfected cells were plated in 6-well plates pre-coated with Matrigel-Matrix hESC-qualified (#354277, Corning, New York, USA) in DMEM/FBS medium. The day after, the medium was replaced with N2B27 medium supplemented with 100 ng/mL βFGF. The medium was changed daily until day 15, when it was substituted with mTeSR1 (#85850, STEMCELL Technologies, Vancouver, BC, Canada). EVOS microscopy system (Thermo Fisher Scientific, Waltham, MA, USA) under a sterile hood was used to pick rounded shaped iPSC colonies and transferred into a 24-well plate for further expansion. Ethylenediaminetetraacetic acid disodium salt dihydrate (EDTA, #S-E1644, Sigma Aldrich) was used for cell dissociation. The study was conducted in compliance with the Code of Ethics of the World Medical Association (Declaration of Helsinki), and in compliance with institutional review board regulations. The study was approved by the Institutional Ethical Committee of the Ospedale Pediatrico Bambino Gesù, Rome (ref. 1410_OPBG_2021, date of approval 11 February 2019). Informed signed consents were obtained from the participating families.

### Fly lines

RNAi fly lines targeting ADSL gene expression (v6343 (w1118; P{GD1722}v6343) and v103823(P{KK108187}VIE-260B)) were obtained from Vienna Drosophila Resource Center. Through Western blotting analysis of RNAi-mediated downregulation of ADSL protein levels in different fly tissues, we focused our studies on v6343 fly RNAi line. Bloomington stock center (http://flybase.bio.indiana.edu/) provided all the GAL4 drivers and other strains utilized: Act-GAL4((y[1] w[*]; P{w[+mC] = Act5C-GAL4}17bFO1/TM6B, Tb[1])

ubiquitous 69B-GAL4 ((w[*]; P{w[+mW.hs] = GawB}69B) which expresses GAL4 panneuronally, in embryonic epiderm and imaginal discs); Mef2-GAL4 ((w[*]; Kr[If-1]/CyO, P{w[+mC] = GAL4-Mef2.R}2, P{w[+mC] = UAS-mCD8.mRFP}2) larval muscles); D-42-GAL4 ((w[*]; P{w[+mW.hs] = GawB}D42) motor neurons); D-42-GAL4,mito-GFP ((w[1118]; P{w[+mW.hs] = GawB}D42, P{w[+mC] = UAS-mito-HA-GFP.AP}3 e[1]/TM6B, Tb[1]) that expresses GFP with a mitochondrial import signal in motor neuron, under D-42 control);ERKCA (y[1] w[*]; P{w[+mC] = UAS-rl[Sem].S}2ERK59CA); ERKWT(w[1118]; P{w[+mC] = UAS-rl.K}2A).

A *Drosophila* strain expressing mito-GFP (w[1118]; P{w[+mW.hs] = GawB}D42, P{w[+mC] = UAS-mito-HA-GFP.AP}3 e[1]/TM6B, Tb[1]) was crossed with w[1118] flies to separate P{w[+mW.hs] = GawB}D42 from P{w[+mC] = UAS-mito-HA-GFP.AP}3, by meiotic recombination. Heterozygous females from the progeny were crossed with a balancer line (w; Sco/CyOTb; MKRS/TM6B) to isolate single recombinant males (w; +/Sco; UAS-mito-HA-GFP/TM6B) without D42-GAL4 (P{w[+mW.hs] = GawB}D42). These recombinant males were crossed with Sp/CyO, P{w[+mC] = GAL4-Mef2.R}2, P{w[+mC] = UAS-mCD8.mRFP}2; MKRS/TM6B females to generate a final stock Mef2-GAL4, UAS-mito-HA-GFP(w; Sco/CyO, P{w[+mC] = GAL4-Mef2.R}2, P{w[+mC] = UAS-mCD8.mRFP}2; UAS-mito-HA-GFP/TM6B) expressing mito-GFP under Mef2-GAL4 control, which was employed to characterize mitochondria quantity and morphology in larva muscle filet preparations. *Drosophila* stocks and crosses were maintained on *Drosophila* standard medium (Nutri-fly Genesee Scientific) at 25°C, unless otherwise indicated.

## METHOD DETAILS

### Cell treatments

Cells were treated with: 70 nM Insulin (Sigma-Aldrich #I9278); 20 ng/μL EGF (Sigma-Aldrich #E5036); Chloroquine (CLQ, Sigma-Aldrich, #C6628). Concanamycin A (ConA, Sigma-Aldrich, #C9705); MG132 (Sigma-Aldrich, #M7449); Cycloheximide (CHX, Sigma-Aldrich, #239765); Dihydroethidium (DHE, Thermo Fisher Scientific #D23107); Adenine (Sigma-Aldrich, #A9795); Guanine (Sigma-Aldrich, #G11950); Cytidine (Sigma-Aldrich, #C4654); Uridine (Sigma-Aldrich, #U3003). The glucose starvation was obtained by washing the cells with phosphate-buffered saline (PBS) (EuroClone, ECB4053) and incubating them with glucose-free DMEM (Thermo Fisher Scientific #11966025) for 24 h. For mitochondrial staining, cells were treated with 50 nM TMRE (Thermo Fisher Scientific #T669); 2 μM JC-1 (5,5′,6,6′-tetrachloro-1,1′,3,3′-tetraethyl-imidacarbocyanine iodide) (Thermo Fisher Scientific #T3168); 50 nM MitoTracker Green FM (Thermo Fisher Scientific #M7514); 100 nM MitoTracker Red CMXRos (Thermo Fisher Scientific #M7512). Cell lines were regularly tested and verified to be mycoplasma negative by PCR; all cell lines tested negative for mycoplasma.

### Transfections

Transfections were performed on SH-SY5Y, and EBV-LCLs. RNAi (RNA Interference) was performed on SH-SY5Y cells and wildtype fibroblasts using Lipofectamine RNAiMAX (Thermo Fisher Scientific #13778075) and 100 pmol of esiRNA targeting human ADSL (Sigma-Aldrich #EHU070001) following the manufacturer's instructions. Stealth RNAi siRNA Negative Control (Thermo Fisher Scientific #12935300) was used as siRNA control. EBV-LCLs were electroporated using Neon Transfection System (Thermo Fisher) following manufacturer instructions and kept o.n. in antibiotics-free medium before being washed and used for further experiments. The following plasmids have been used: p3xFlag-CMV7-Erk2 (Addgene #39223; ERK-Wt) and p3xFlag-CMV7-Erk2-L73P-S151D (ERK2-CA), kind gift of prof. Issam Ben-Sahra.[26]

### Western blotting (WB)

Cells were lysed in RIPA buffer (50 mM Tris-HCl pH 7.4, 1% Triton X-100, 150 mM NaCl, 0.25% Sodium deoxycholate, 0.1% SDS, 1 mM EDTA and 5 mM $MgCl_2$) supplemented with: protease inhibitor cocktail (PIC) (Sigma-Aldrich #P8340); 10 mM β-glycerophosphate (Sigma-Aldrich #G9422), 0.2 mM $Na_4VO_3$ (Sigma-Aldrich #S6508) and 5 mM NaF (Sigma-Aldrich #201154). For *Drosophila melanogaster*, third-instar larvae were collected and homogenized using a glass potter to enhance tissue dissociation. Protein extraction was carried out using the same RIPA buffer described above. Lysates were incubated for 30′ on ice and then centrifuged at 13.000 rpm, at 4°C, for 10'. Proteins from fly heads expressing the indicated constructs under *eyeless*-GAL4, were extracted in 2% SDS buffer (supplemented with protease and phosphatase inhibitors). Protein concentrations were determined with Folin-Lowry assay (DC Protein assay, Bio-Rad #5000111) and BCA (Bicinchoninic Acid) assay (Pierce BCA Protein Assay Kit, Thermo Fisher Scientific #23225). Samples were denatured by adding 1 volume of 4X Sample Buffer (4% SDS, 20% glycerol, 0.004% bromophenol blue, 125 mM Tris-HCl pH 6.8, 10% β-mercaptoethanol) and incubated at 95°C for 10'. Then, proteins were separated by SDS-PAGE. PVDF (Merck Millipore #IPVH00010) membranes were incubated with primary antibodies followed by horseradish peroxidase-conjugated secondary antibody (Bio-Rad, rabbit #1706515, mouse #1706516) and visualized with ECL (Merck Millipore #WPKLS0500). Densitometry analysis was performed using ImageJ software. Comparison between control and sample in the WB intensity measurement was made from the same WB.

### Antibodies

The primary antibodies used in this study were as follows: *p*-AKT Thr308 (Cell Signaling Technology #9275, WB 1:1000); AKT (Cell Signaling Technology #9272, WB 1:1000); *p*-ERK1/2 (Thr202/Tyr204) (Cell Signaling Technology #9101, WB 1:1000); ERK1/2 (Cell Signaling Technology #9102, WB 1:1000); ADSL (C-11) (Santa Cruz Biotechnology #sc-365623, WB 1:1000), GAPDH (6C5) (Santa

Cruz Biotechnology #sc-32233, WB 1:1000), HSP90α/β (F-8) (Santa Cruz Biotechnology #sc-13119, WB 1:3000), TOM20 (F-10) (Santa Cruz Biotechnology #sc-17764, WB 1:1000, IF 1:200); UBIQUITIN (Santa Cruz Biotechnology #sc-8017, WB 1:1000); ACTIN (Sigma-Aldrich #A2066, WB 1:3000); OxPhos Human antibody cocktail (Thermo Fisher Scientific #45–8099); SYN (3C11 (anti SYNORF1) Developmental Studies Hybridoma Bank, US, WB 1:1000); Giotto ([56] was a gift from GL Cestra; https://www.antibodyregistry.org/AB_2892585, WB 1:3000); HRP (Peroxidase AffiniPure Rabbit Anti-Human IgG (H + L), Jackson ImmunoResearch #309-035-003); Discs large (4F3 anti-discs large, Developmental Studies Hybridoma Bank, US, IF 1:200); LC3B (D11, XP, Cell Signaling Technology #3868, WB 1:1000); Cyclin B1 (Cell Signaling Technology #4138, WB 1:1000); OPA1 (Cell Signaling Technology #80471, WB 1:1000); *p*-DRP1 Ser616 (Cell Signaling Technology #3455, WB 1:1000); DRP1 (Cell Signaling Technology #8570, WB 1:1000); MFN2 (Santa Cruz Biotechnology #sc-515647, WB 1:1000); FLAG (M2, Sigma-Aldrich #F1804, WB 1:1000).

### Mitochondrial mass and transmembrane potential analysis

EBV-LCL cells were incubated with 50 nM MitoTracker Green FM for 20′ to measure mitochondrial mass, or with 50 nM TMRE or 2 μM JC-1 for 25′ to measure mitochondrial transmembrane potential. For mitophagy flux analysis, before MitoTracker Green FM staining, cells were incubated with Chloroquine 40mM (Sigma-Aldrich #C6628) for 4h. The superoxide levels were measured by using Dihydroethidium (Invitrogen, D1168), 5 μM for 20'. The cells were subsequently collected and washed with PBS before the flow cytometer analysis.

### Oxygen consumption measurements

Mitochondrial function and ATP production rates were assessed using the Seahorse XFe96 Analyzer (Agilent Technologies). Two assays were performed: the Mito Stress Test and the ATP Real-Time Rate Assay (Agilent #103015-100), which allow the measurement of both ECAR (Extracellular Acidification Rate) and OCR (Oxygen Consumption Rate). EBV-LCL cells, human primary fibroblasts, or SH-SY5Y cells were seeded into Agilent Seahorse microplates (#101085-004) in 100 μL per well using their standard culture media. Prior to the assay, the medium was replaced with 180 μL of minimal assay medium supplemented with 1 mM pyruvate, 10 mM glucose, and 2 mM glutamine, adjusted to pH 7.4. The plate was then incubated for 40 min at 37°C in a $CO_2$-free incubator. The XF Cell Mito Stress Test evaluates key aspects of mitochondrial function by measuring OCR. It provides insights into mitochondrial dysfunction and underlying metabolic changes. The following compounds were sequentially injected during the assay: 1 μM Oligomycin, 1 μM FCCP (Carbonyl cyanide-4-(trifluoromethoxy) phenylhydrazone), 0.5 μM Rotenone and Antimycin A. For the ATP Real-Time Rate Assay, the analysis was performed following sequential injections of: 1.5 μM Oligomycin, 0.5 μM Rotenone +0.5 μM Antimycin A. This assay measures overall ATP production rates and differentiates between ATP produced via mitochondrial oxidative phosphorylation (OXPHOS) and glycolysis, the two primary ATP-generating pathways. Post-acquisition, OCR and ECAR data were converted to ATP production rates using the Agilent XF Real-Time ATP Rate Assay Report Generator. The percentage contribution of each pathway was calculated using the following formulas: % Mitochondrial ATP (OXPHOS) = (Mitochondrial ATP production rate/Total ATP production rate) × 100; % Glycolytic ATP = (Glycolytic ATP production rate/Total ATP production rate) × 100.

Data analysis was conducted using Seahorse Wave Desktop Software, and statistical analyses were performed with GraphPad Prism 6.

### Immunofluorescence and confocal analysis

For the fibroblasts, in order to facilitate the cell adhesion to the coverslips, their surface was treated with 5 μg/mL fibronectin (Sigma-Aldrich #F2006) for 2 h at 37°C. After two PBS washes, the cells were seeded at 30% confluence. Cells were fixed with 4% formaldehyde solution (Sigma-Aldrich #252549) in PBS for 15′ at RT. Cells were permeabilized with 0.1% Triton X-100 (Sigma-Aldrich #T8787) diluted in PBS for 10′ at RT. Coverslips were incubated with a solution of primary antibodies diluted in PBS and 3% Normal Goat Serum (NGS) (Thermo Fisher Scientific #31872) O/N at 4°C. Cells were incubated with a solution of secondary fluorescent antibodies anti-rabbit IgG (Thermo Fisher Scientific #A21430 or #A11070, as reported in the figure legends) and anti-mouse IgG (Thermo Fisher Scientific #A11017 or #A21425, as reported in the figure legends) diluted 1:500 in PBS and 3% NGS for 1 h, at 4°C. For mitochondrial staining, fibroblasts were incubated with 100 nM MitoTracker Red CMXRos (Thermo Fisher Scientific, #M7512) for 25 min at 37°C. Following incubation, cells were washed twice with PBS to remove excess dye and then fixed using the protocol described above. Cell nuclei were stained with 1 μg/mL Hoechst (Thermo Fisher Scientific #H3570) for 10′ at RT. Coverslips were closed with an aqueous mounting medium (Fluoromount Aqueous Mounting Medium, Sigma-Aldrich #F4680). The images were acquired utilizing either a Zeiss LSM 800 confocal microscope (Zeiss, Oberkochen, Germany) outfitted with an Objective Plan-Apochromat 63x/1.4 employing an AiryScan module (as detailed in the figure legend) or a Leica TCS-SP8X laser-scanning confocal microscope (Leica Microsystems, Mannheim, Germany) equipped with a 60x (NA 1.4). The images acquired with the Zeiss 800 microscope were subjected to processing using the ZEN 3.1 Blue Edition software (Zeiss, Oberkochen, Germany). This program was utilized to generate AiryScan images, which were then processed using the deconvolution tool. For confocal analysis of IPS cells or motor neurons, cell were fixed and blocked as described above. Polyclonal or monoclonal primary antibodies against the following were used: 1:200 mitochondria antibody (MTC02, #NB600-556, Novus Biologicals, Centennial, CO, USA) overnight, and 1:500 βIII-Tubulin antibody (#T2200, Sigma-Aldrich) for two hours. Cells were then incubated with secondary antibodies conjugated with Alexa Fluor 488 (#A11070, Thermo Fisher Scientific) or Alexa Fluor 555 (#A-21425, Thermo Fisher Scientific) and diluted 1:500 in PBS.

Nuclei were stained with [1 μg/mL] Hoechst (#33342, Thermo Fisher Scientific) for 10 min at RT, and coverslips were mounted using 1:1 PBS/glycerol. All images were acquired using the confocal microscope Leica Stellaris (Leica Microsystems, Wetzlar, Germany) with 63x magnification in combination with the LAS-X software (Leica Microsystems, Wetzlar, Germany). Muscle filets from *Drosophila* third-instar larvae were dissected according to standard protocols (Brent et al., 2009a, 2009b; Wu and Luo, 2006). Briefly, larvae were dissected in PBS and fixed in 4% paraformaldehyde, 4% sucrose at RT for 1 h. After three washes in PBS, filets were permeabilized in PBST (1% Triton X-100) 10′ at RT and then incubated with primary antibody diluted in blocking buffer (PBS, 0.1% Triton X-100, 2% BSA) overnight at 4°C in a wet chamber. Samples were then incubated with anti-mouse or anti-rabbit TRITC (Jackson ImmunoResearch, UK) for 1 h at RT. Preparations were mounted in antifade mounting medium with DAPI (VECTASHIELD, Vector Laboratories, US). In order to label motor neuron axons or larva muscle fibers, samples were labeled for 1 h at RT in blocking buffer with anti-Horseradish Peroxidase (1:300, Alexa Fluor 488 AffiniPure Goat, Jackson ImmunoResearch, UK) or Rhodamine Phalloidin (1:200, Cytoskeleton, Inc, US), respectively. Confocal imaging was performed either on a Leica or Zeiss microscopes. Leica TCS-SP8X laser-scanning confocal microscope (Leica Microsystems, Mannheim, Germany) was equipped with tunable white light laser (WLL) source. Sequential confocal images on Leica were acquired using a 63x oil-immersion objective (1.40 NA) with a 1,024 × 1,024 format, z-step size of 0.5–1 μm, and with an electronic zoom magnification up to 2.0. Z-reconstructions were imported into LASX 3D Analysis (Leica Microsystems) software to obtain their maximum projections. Sequential confocal images from LSM 700 confocal microscope (Zeiss, Oberkochen, Germany) were acquired using a 63x oil-immersion objective with a 1,024× 1,024 format, z-step size of 0.5–1 μm, and with an electronic zoom magnification up to 2.0. Images were imported into ZEN 3.1 Blue Edition (Carl Zeiss Microscopy GmbH, Germany) software to obtain best fit maximum projections. The images were analyzed using the Fiji version of the ImageJ software (NIH). The ImageJ software was also used to quantify immunofluorescence intensity of the neuronal marker to study the efficiency of neuronal differentiation. Cells positive to the βIII-Tubulin marker, were counted and compared to the total number of cells.

### Analysis of mitochondrial network distribution

In fibroblast cells, mitochondria were stained with MitoTracker Red CMXRos. Quantitative analysis of mitochondrial morphology was performed using the "Analyze Particles" function in ImageJ software on thresholded images. Among the available shape descriptors, we calculated circularity (Circ.) and aspect ratio (AR). Circularity was computed as $4\pi \times \text{area/perimeter}^2$ where a value of 1.0 represents a perfect circle and values approaching 0.0 indicate increasingly elongated shapes. AR was calculated as the ratio of the major axis to minor axis of each particle, with higher values indicating greater elongation. To selectively analyze small circular mitochondrial fragments, we applied a particle size range of 33–3333 pixels and a circularity range of 0.4–1.0. In motoneurons, each sample was analyzed by calculating fluorescence intensity levels of the mitochondrial marker MTC02 (#NB600-556, Novus Biological, Centennial, CO, USA) on three different portions of the selected neurites, considering the βIII-Tubulin signal. Specifically, neuronal cells were manually divided into three areas: cell body, proximal area, and distal area. For each segment, the fluorescence intensity levels with respect to the considered area, were calculated using ImageJ (NIH). In *Drosophila*, maximum projections of mito-GFP fluorescence images from 5 to 10 independent confocal stacks for each genetic background were binarized, automatically thresholded and subjected to stringent particle analysis. To identify only the small circular fragments of mitochondria narrow parameters were chosen (range of pixel unit 33–3333; circularity range of 0.4–1). Quantitative analysis of neuromuscular junction marker accumulation was performed on images with a manual method based on the delimitation of pre- and post-synaptic margins, using Fiji/ImageJ software.

### Positivity to alkaline phosphatase test

To assess pluripotency of the selected ADSL clones, alkaline phosphatase (ALP, #86R-1, Merck KGaA, Darmstadt, Germany) test was employed. Cells, previously fixed on glasses in 4% formaldehyde, methanol free (#28908, ThermoFisher Scientific), were incubated for 40 min at RT with a solution based on naphthol AS-BI and fast red violet LB (#86R-1KT, Sigma Aldrich, St. Louis, MO, USA). Cells were then washed with phosphate-buffered saline (PBS, #PBS-1A, Capricorn Scientific) and coverslips were mounted using a solution containing PBS/Glycerol (#G6279, Sigma Aldrich). Images were captured using a Leica DM1000 (Leica Microsystems, Wetzlar, Germany) equipped with Leica LAS X software (Leica Microsystems, Wetzlar, Germany) and representative images were composed in an Adobe Photoshop CS6 format (Adobe Systems Inc., San Jose, CA, USA).

### Immunofluorescence analysis to test pluripotency

For immunofluorescence analyses, cells were fixed in 4% formaldehyde for 10 min at room temperature (RT), washed with PBS, and blocked with 5% bovine serum albumin (#A8022, Sigma Aldrich) and 0.1% Triton X-100 (#9002-93-1, Sigma-Aldrich). The following primary antibodies were used: rabbit monoclonal antibody against OCT-4 (1:400, #MA5-14845, Invitrogen), rat monoclonal antibody against SOX-2 (1:100, #BMS14-9811-82, Invitrogen, eBioscience), mouse against SSEA4 (1:250, #MA1-021, Invitrogen), mouse against TRA1-60 (1:100, sc-21705, Santa Cruz Biotechnology). Cells were then incubated with the appropriate secondary antibodies, conjugated with Alexa Fluor 488 or Alexa Fluor 555 (#A-21430, #A-11017, #A-21425, and #A-11006, Invitrogen). Nuclei were stained with 1 μg/mL Hoechst (#33342, Invitrogen), and slides were observed in an inverted Leica DMi8 microscope. Images were captured by Leica Application Suite software, and representative figures were composed using Adobe Photoshop CS6 (Adobe Systems Inc., San Jose, CA, USA).

### DNA sequencing to confirm the mutations following reprogramming

Pellets from each ADSL patient, obtained by centrifuging EDTA-detached cells at 1200 rpm for 5 min, were processed for genomic DNA extraction using MagPurix Culture Cell DNA extraction kit, following manufacturer's instructions (#ZP02005, Zinexts Life Science) and processed by MagPurix 12s extractor (Zinexts Life Science). The coding sequence of ADSL gene was amplified by PCR specific primers using KAPA2G Fast ReadyMix Kit (#S-KK5101, Sigma Aldrich). Amplimers were sequenced using SANGER (SeqStudio, ThermoFisher Scientifics).

### Karyotype check following reprogramming

To check the genome integrity of the obtained iPSC clones, hPSC Genetic Analysis Kit (#07550, Stem Cell Technology) was employed. This qPCR-based kit enables the genetic screening of the human iPSC lines analyzing samples in triplicate, using double-quenched probes with a 5-carboxyfluorescein (5-FAM) dye. The kit allow to detect the critical minimal regions of the 8 most commonly mutated regions and a genomic DNA control is provided with demonstrated normal copy number over the regions of interest. DNA from each sample was processed following step-by-step manufacturer's instructions, and the obtained Cq values were analyze using the Online Genetic Analysis Application available at www.stemcell.com/geneticanalysisapp.

### Trilineage differentiation potential

STEMdiffTrilineage Differentiation Kit (#05230, Stem Cell Technologies) was used to functionally validate the ability of the obtained iPSCs to differentiate into the three germ layers: ectoderm, mesoderm, and endoderm. A specific number of cells were plated on glasses in 6-well plates pre-coated with Matrigel, and different media were used to induce the endoderm, ectoderm, or mesoderm differentiation. Glasses were fixed in 4% PFA and cells were stained to assess their differential potential using the following antibodies: anti-SOX17 (1:3.200, #81778, Cell Signaling, Danvers, MA, USA), anti-NCAM (1:400, #89861, Cell Signaling) and anti-Brachyury (1:1.600, #81694, Cell Signaling). Images were captured by an inverted Leica DMi8 microscope using a Leica Application Suite software.

### JC-1 staining

5,5,6,6′-Tetrachloro-1,1′,3,3′-tetraethylbenzimidazolylcarbocyanine chloride (JC-1) (T3168, Life Technologies, Carlsbad, CA, USA) probe was used to study mitochondrial membrane potential (MMP) of ADSL iPSCs. Cells cultured in mTeSR1 medium, were treated with [5 μM] JC-1 for 30 min at 37°C 5% CO2. After washing twice with the culturing medium, images were captured before and after 1, 5, 10, 15, and 30 min following [10 μM] H 2 O 2 exposure, using an inverted Leica DMi8 microscope (Leica) where CO2 (5%) and temperature (37°C) were controlled using a Top Stage Incubator (Okolab Srl, Italy) during the experiments. Representative images for each time points were chosen to compose the figure using Adobe Photoshop CS6 (Adobe Systems Inc., San Jose, CA, USA).

### Motor neurons differentiation

Cells were differentiated into motor neurons following the protocol described in Corti et al.[57]

### Morphometric analysis using incucyte SX5 live cell analysis software

Morphometric analysis of motor neurons was performed using the Incucyte Neurotrack software module. 10.000 cells were plated on pre-coated with Matrigel 96-well plates (#Z707910, TPP tissue culture plates, Merck KGaA, Darmstadt, Germany) at day 10 of motor neuron differentiation. Cell culture medium was changed according to the protocol described in the previous paragraph. The software allowed to automatically process Incucyte images and to analyze neurite dynamics without labels in living cells in each well of a 96-plates. The algorithm masked and quantified each image, giving information about neurite length, branch points, and cell body area. The analyses of neurite length ($mm/mm^2$) were performed directly on phase contrast images from day 25 to day 30 of neuronal differentiation and scans were performed every 2 h with 10x magnification.

### TUNEL assay

The DeadEnd Fluorometric TUNEL System (#G3250, Promega, Fitchburg, USA) was used for the specific detection and quantitation of ADSL apoptotic cells at day 0, day 10 and day 30 of motor neurons differentiation. TUNEL assay measured the fragmented DNA of apoptotic cells by catalytically incorporating fluorescein-12-dUTP at 3′-OH DNA ends using Terminal Deoxynucleotidyl Transferase (TdT), which forms a polymeric tail using the principle of the TUNEL (TdT-mediated dUTP Nick-End Labeling) assay. The fluorescein-12-dUTP-labeled DNA was visualized directly by fluorescence microscopy and the number of apoptotic cells (expressing green fluorescence) were manually counted and related to the total number of cells, whose nuclei were stained with [1 μg/mL] Hoechst (#33342, Invitrogen).

### Analysis of cell viability and apoptosis in iPSCs

Cells were stained with 50 mg/mL propidium iodide before analysis by a BD FACSVerse instruments (BD Biosciences). Apoptotic cells were evaluated by calculating peak areas of hypodiploid nuclei in previously premeabilized cells (sub-G1).

### Analysis of mitochondrial network distribution in iPSCs

For mitochondrial analyses, each sample was analyzed by calculating fluorescence intensity levels of the mitochondrial marker on three different portions of the selected neurites, considering the βIII-Tubulin signal. Specifically, neuronal cells were manually divided into three areas: cell body, proximal area, and distal area. For each segment, the fluorescence intensity levels with respect to the considered area, were calculated using ImageJ (NIH).

### Metabolite extraction from cells

Human primary fibroblasts were washed twice with PBS. The plates were put on dry ice adding 500 μL of extraction solution per million cell. The extraction reagent was composed of 50% LC-MS grade Methanol (Thermo Fisher Scientific #10284580), 30% LC-MS grade Acetonitrile (Thermo Fisher Scientific #10001334), 20% ultrapure water (Sigma-Aldrich #270733) and 5 μM Valine-d8 (CK isotopes #DLM-488, as internal standard). The plates were incubated for 20′ on a dry ice-methanol bath to break cell membranes. Cells were scrapped off the plates and transferred into pre-chilled tubes. The cell extract suspension was, then, shaken for 15′ at 4°C in at maximum. The samples were centrifuged for 20′ at 4°C at maximum speed (13000 rpm or higher). Only the top 80% of the supernatant was collected and put into pre-labelled autosampler vials (Sigma-Aldrich #29659-U). A pooled sample was also prepared by taking 10 μL of each sample. The samples were stored −80°C until analysis.

### pHILIC LC-MS method

HILIC chromatographic separation of metabolites was achieved using a Millipore Sequant ZIC-pHILIC analytical column (5 μm, 2.1 × 150 mm) equipped with a 2.1 × 20 mm guard column (both 5 μm particle size) with a binary solvent system. Solvent A was 20 mM ammonium carbonate, 0.05% ammonium hydroxide; Solvent B was acetonitrile. The column oven and autosampler tray were held at 40°C and 4°C, respectively. The chromatographic gradient was run at a flow rate of 0.200 mL/min as follows: 0–2 min: 80% B; 2–17 min: linear gradient from 80% B to 20% B; 17–17.1 min: linear gradient from 20% B to 80% B; 17.1–22.5 min: hold at 80% B. Samples were randomized and analyzed with LC–MS in a blinded manner with an injection volume was 5 μL. Pooled samples were generated from an equal mixture of all individual samples and analyzed interspersed at regular intervals within sample sequence as a quality control. Metabolites were measured with a Thermo Scientific Q Exactive Hybrid Quadrupole-Orbitrap Mass spectrometer (HRMS) coupled to a Dionex Ultimate 3000 UHPLC. The mass spectrometer was operated in full-scan, polarity-switching mode, with the spray voltage set to +4.5 kV/-3.5 kV, the heated capillary held at 320°C, and the auxiliary gas heater held at 280°C. The sheath gas flow was set to 55 units, the auxiliary gas flow was set to 15 units, and the sweep gas flow was set to 0 unit. HRMS data acquisition was performed in a range of m/z = 70–900, with the resolution set at 70,000, the AGC target at 1 × 10 6, and the maximum injection time (Max IT) at 120 ms. Metabolite identities were confirmed using two parameters: precursor ion m/z was matched within 5 ppm of theoretical mass predicted by the chemical formula; the retention time of metabolites was within 5% of the retention time of a purified standard run with the same chromatographic method. Chromatogram review and peak area integration were performed using the Thermo Fisher software Tracefinder 5.0 and the peak area for each detected metabolite was normalized against the total ion count (TIC) of that sample to correct any variations introduced from sample handling through instrument analysis. The normalized areas were used as variables for further statistical data analysis. For $^{13}$C-glycine tracing analysis, the theoretical masses of isotopes were calculated and added to a library of predicted isotopes. These masses were then searched with a 5-ppm tolerance and integrated only if the peak apex showed less than 1% difference in retention time from the [U-$^{12}$C] monoisotopic mass in the same chromatogram. After analysis of the raw data, natural isotope abundances were corrected using the AccuCor algorithm (https://github.com/lparsons/accucor).

### Real-Time PCR

Total DNA was isolated using the QIAGEN DNeasy Blood and Tissue Kit (Qiagen #69504) according to manufacturer's protocol. Total RNA was isolated using the ReliaPrep kit RNA Miniprep Systems (Promega #Z6011) following the manufacturer's instructions, and 2 μg RNA were retrotranscribed using M-MLV enzyme and oligodT (Promega #C1101). Real-Time PCR was performed using SYBR Green (SYBR Green PCR Master Mix; Thermo Fisher Scientific #4309155) and took place into the QuantStudio 3 System (QuantStudio 3 real-time PCR System, 96-well, 0.2 mL, laptop; Thermo Fisher Scientific #A28567) with the following program: 95°C, 10'; 95°C 15''; 60°C, 1'; 95°C, 15''; 60°C, 1'; 95°C, 15''. The second and third steps were repeated 40 times. The following oligonucleotide primers were used for: ADSL (5′- GGAGATGTGCTTCGTGTTTAG-3'; 5′- GTCGATGTTCTCCAGGTTTG-3′); HPRT1 (5′- CTGAGGATTTGGAAAGGGTG-3'; 5′- CAGAGGGCTACAATGTGATG-3′); COXII (5′-TGCCCGCCATCATCCTA-3'; 5′-TCGTC TGTTATGTAAAGGATGCGT-3′); ATP6 (5′- ACACCCCTTATCCCCATACTAG-3′, 5′-ATGGTTGATATTGCTAGGGTGG-3′); ND3 (5′-AGAAAAATCCACCCCTTACGGT-3'; 5′-TGGAGAAAGGGACGCGG-3′); B2M (5′-CTCCGTGGCCTTAGCTGTG-3′, 5′-TCTCTGGAT GACGTGAG-3′). The mRNA expression of the gene of interest was normalized to HPRT1 or B2M expression, and the ΔΔCt method was used; mRNA levels were then normalized to the control conditions.

### Mitochondrial DNA (mtDNA) copy number quantification

Total DNA was isolated using the QIAGEN DNeasy Blood and Tissue Kit (Qiagen #69504) according to manufacturer's protocol. Real-Time PCR was performed using SYBR Green (SYBR Green PCR Master Mix; Thermo Fisher Scientific #4309155) and took place into the QuantStudio 3 System (QuantStudio 3 real-time PCR System, 96-well, 0.2 mL, laptop; Thermo Fisher Scientific #A28567) with the

following program: 95°C, 10'; 95°C 15''; 60°C, 1'; 95°C, 15''; 60°C, 1'; 95°C, 15''. The second and third steps were repeated 40 times. The following oligonucleotide primers were used for: *ACTB* gene (5′-CCCCTGGCGGCCTAAGGACT-3'; 5′-ACATGCCGGAGC CGTTGTCG-3'); D loop (5′-ACCACCCAAGTATTGACTCACC-3'; 5′-CCGTACAATATTCATGGTGGCT-3'); *MT-ND1* (5′-TTCTCC GATCCGTCCCTAACA-3'; 5′-GGTTGTCCTCCGATTCAGGTT-3'). The DNA abundance of the gene of interest was normalized to genomic *ACTB* expression, and the ΔΔCt method was used; DNA levels were then normalized to the control conditions.

### GeneBridge analysis

To explore additional functional associations of ADSL beyond its canonical role in purine metabolism, we performed a GeneBridge correlation analysis. GeneBridge is a large-scale, transcriptome-based integrative platform that leverages thousands of publicly available RNA-seq datasets across diverse human tissues and cell types to uncover gene-to-pathway relationships through expression-based correlation analysis.[15] We queried the expression profile of ADSL across the GeneBridge database and assessed its correlation with curated gene sets representing biological processes in muscle and the nervous system. Gene set enrichment was performed using predefined Hallmark and Gene Ontology (GO) terms. Positive and negative correlation scores were used to infer upregulated or downregulated associations between ADSL expression and cellular pathways.

### Climbing assay

Negative geotaxis assays were performed according to the standard protocols[58] and the climbing performance of each fly population (around 100 male flies 2–5 days after eclosion per genotype) was represented plotting the average distance climbed at the indicated time.

## *DROSOPHILA* EYE AREA QUANTIFICATION

Adult fly eyes from animals expressing either ADSL RNAi construct #103823 or #6343 under the control of the eyeless-GAL4 driver at 29°C were imaged to assess eye morphology. Flies were anesthetized and imaged using a ZEISS Stemi 508 stereomicroscope equipped with an Axiocam 105 color camera, at 50X magnification. Images were acquired using ZEISS ZEN Blue software (version 3.1) under standardized settings across all genotypes. Eye area was measured using ImageJ FIJI (NIH freeware). Each eye was manually outlined, and the area (in pixels) was calculated using the "Measure" function. Measurements from control fly eyes were pooled, and comparisons between groups were performed.

### Neuromuscular junction (NMJ) morphology analysis in Drosophila larvae

Third-instar larvae expressing ADSL RNAi (#6343) under the Mef2-GAL4 driver were reared at 29°C and dissected for immunofluorescence (IF) analysis of neuromuscular junctions (NMJs) on muscle 6 and 7. Preparations were co-stained with fluorescently labeled phalloidin to visualize muscle actin fibers and with an antibody against Discs large, a marker of the subsynaptic reticulum. Discs large signal intensity was quantified from confocal images using ImageJ software and normalized to the total NMJ area. A total of 9 control NMJs and 12 ADSL RNAi NMJs were analyzed. For Bouton morphology, third-instar larvae expressing ADSL RNAi (#6343) under the control of the Mef2-GAL4 driver were dissected and fixed for immunofluorescence (IF) analysis of neuromuscular junctions (NMJs). NMJs were examined on muscle 6/7 (primary analysis) and muscle 12/13 (additional representative examples). Presynaptic membranes were labeled using an anti-HRP antibody, and images were acquired using confocal microscopy under identical settings across genotypes. Bouton morphology was quantified by measuring the total bouton area per NMJ and normalizing it to the junction length. Additionally, abnormally large boutons were defined by a fixed threshold (area >1000 a.u.) and the cumulative area per NMJ was calculated. At least 19 NMJs per genotype were analyzed.

### β-Galactosidase assay

Briefly, we used mammal β-Galactosidase assay kit from Thermo Scientific (#75707) according to manufacturer's instructions. The β-Galactosidase reading was conducted six times for each cell line and subsequently integrated with the Cristal Violet test for the purpose of normalization. Hence, the observed outcome is determined by calculating the ratio between the absorbance of β-Galactosidase at a wavelength of 405nm and the absorbance of Cristal Violet at a wavelength of 592nm. All measurements were standardized relative to the control group.

### Electron microscopy analysis

Body-wall muscles from L3 larvae were dissected and fixed overnight at 4°C in 2% paraformaldehyde, 2.5% glutaraldehyde and 0.1 M Sodium cacodylate buffer pH 7.4. After rinsing in 0.1 M cacodylate buffer with 1% tannic acid, the samples were postfixed in 1:1 of 2% OsO4 and 0.2 M cacodylate buffer for 1 h. The samples were rinsed, dehydrated in an ethanol series, and embedded in an epoxy resin (Sigma-Aldrich). Ultrathin sections were obtained with an Ultrotome V (LKB) ultramicrotome, counterstained with uranyl acetate and lead citrate and viewed with a Tecnai G2 (FEI) transmission electron microscope. Images were captured with a Veleta (Olympus Soft Imaging System) digital camera.

## QUANTIFICATION AND STATISTICAL ANALYSIS

Densitometry analysis was performed using ImageJ software. All statistical analyses were performed using the GraphPad Prism 9 or 10 software. Statistical parameters including the exact value of n, type of replicates, statistical tests, error bars, and significance are reported in all associated figure legends. Shapiro-Wilk test was used for checking the normality distribution of the values for each condition: a) in case of two conditions, the parametric test was unpaired Student's t-test and the non-parametric test was Mann-Whitney test, b) in case of more than two conditions, the parametric test was one/two-way ANOVA and the non-parametric test was Kruskal-Wallis test. When the control group was set equal to 1, the Wilcoxon signed-rank test or Friedman test was used for non-parametric data, as appropriate to account for paired sample designs. two-way ANOVA was used in separate analyses involving two independent variables. For pairwise multiple comparisons, we performed the following post hoc tests: Dunnett's test after one-way ANOVA, Tukey's test after two-way ANOVA, and Dunn's test following Kruskal–Wallis or Friedman tests. The statistical details of each experiment—including the tests performed, the exact value of n, a definition of what n represents, and measures of precision (e.g., mean and SEM)—are provided in the respective figure legends.